

Field measurements demonstrate distinct initiation and cessation thresholds governing aeolian sediment transport flux

Raleigh L. Martin*, Department of Atmospheric and Oceanic Sciences, University of California, Los Angeles, CA 90095

Jasper F. Kok, Department of Atmospheric and Oceanic Sciences, University of California, Los Angeles, CA 90095

Key Points

1. We provide the first field-based evidence for separate fluid and impact thresholds in aeolian saltation
2. Saltation occurrence is mediated by both thresholds, but fluid (impact) threshold dominates during infrequent (near-continuous) transport
3. Both thresholds are important for high-frequency saltation prediction, but long-term aeolian fluxes are governed mostly by impact threshold

*raleighm@atmos.ucla.edu

Abstract

Wind-blown sand and dust models depend sensitively on the threshold wind stress. However, laboratory and numerical experiments suggest the coexistence of distinct “fluid” and “impact” thresholds for the initiation and cessation of aeolian saltation, respectively. Because aeolian models typically use a single threshold, existence of dual thresholds produces ambiguous predictions of wind-driven transport. Here, we derive the first field-based estimates of distinct fluid and impact thresholds from high-frequency saltation measurements at three field sites, and we determine how these thresholds control the occurrence of saltation. We show that, when saltation is mostly inactive, its instantaneous occurrence is governed primarily by wind exceedance of the fluid threshold. As saltation activity increases, so too does the relative importance of the impact threshold, until it dominates under near-continuous transport conditions. Although both thresholds are thus important for high-frequency saltation prediction, we find that the time-averaged saltation flux is primarily governed by impact threshold.

1. Introduction

Determining the threshold wind shear stress for the occurrence of wind-driven (“aeolian”) sand transport has been a central challenge for studies of planetary, coastal, and desert aeolian processes [e.g., *Bagnold*, 1941; *Iversen and White*, 1982; *Shao and Lu*, 2000]. In desert and semi-arid environments, the aeolian saltation threshold regulates the frequency of topsoil erosion and mineral dust emission [e.g., *Rice et al.*, 1999]. Where sand dunes and ripples are present, the saltation threshold governs the frequency of migration of these bedforms [e.g., *Fryberger et al.*, 1979]. Aeolian transport studies indicate that sand flux scales linearly [e.g., *Martin and Kok*, 2016] or to the $3/2$ power [e.g., *Bagnold*, 1941] of wind stress in excess of the saltation threshold, so slight shifts in the presumed threshold value can profoundly change predictions of the total sand saltation flux and associated dust emissions [e.g., *Sherman et al.*, 2013; *Kok et al.*,

2014; *Webb et al.*, 2016]. Uncertainty in threshold is therefore a major issue for studies relating aeolian transport observations to atmospheric conditions on Earth [e.g., *Lindhorst and Betzler*, 2016], Mars [e.g., *Bridges et al.*, 2012; *Ayoub et al.*, 2014] and other planetary surfaces [e.g., *Lorenz and Zimbelman*, 2014].

Despite the central importance of the saltation threshold in predicting sand and dust fluxes, there remains a lack of agreement over the best way to model or even measure this threshold [*Barchyn and Hugenholtz*, 2011]. Predictive equations for saltation (and the resulting dust emission) usually include a single threshold value [*Barchyn et al.*, 2014b], traditionally the “fluid threshold” shear stress τ_{ft} for initiating saltation transport solely by aerodynamic forces [*Bagnold*, 1941; *Iversen and White*, 1982; *Marticorena and Bergametti*, 1995]. However, theory and measurements suggest the presence of a separate, lower “impact threshold” shear stress τ_{it} required to sustain saltation through saltator impacts with the soil bed. This impact threshold has been hypothesized to equal the rate of momentum dissipation at the surface [*Owen*, 1964], which is controversial [*Kok et al.*, 2012], but for which there is now limited experimental support [*Walter et al.*, 2014]. Based on its role in the momentum balance, most recent saltation models therefore use impact threshold as the zero-intercept value for the saltation flux [*Ungar and Haff*, 1987; *Creysseles et al.*, 2009; *Martin and Kok*, 2016].

Though using a single threshold for saltation modeling is convenient, path-dependent turbulent wind fluctuations around impact and fluid thresholds have been proposed to cause intermittent saltation transport that displays hysteresis [*Kok*, 2010b]. The ratio of impact and fluid thresholds governing hysteresis depends on the relative importance of collisions versus direct fluid drag for particle entrainment: collision entrainment increases with particle-fluid density ratio, while fluid entrainment increases with gravitational acceleration [*Kok*, 2010b; *Pächt and Durán*, 2016]. On Earth, the experimentally [*Bagnold*, 1937] and numerically [*Kok*, 2010b] predicted ratio of impact and fluid threshold shear velocities u_{*it}/u_{*ft} is approximately 0.8, whereas u_{*it}/u_{*ft} is predicted to be as low as 0.1 on Mars [*Kok*, 2010a].

Despite the potential importance of both fluid and impact thresholds in saltation modeling, field studies have not yet confirmed the existence of two separate thresholds, let alone determined which should be used for modeling sand and dust flux. Field-based determinations of fluid and impact threshold have been hindered by the generally poor correlation between time series of wind speed and saltation flux at short time scales [e.g., *Wiggs et al.*, 2004; *Davidson-Arnott et al.*, 2005; *Davidson-Arnott and Bauer*, 2009], partially due to the necessity of spatially separating saltation and wind measurements [*Baas*, 2008]. Even if measurements could be directly co-located, variability of instantaneous threshold would still occur due to the chaotic nature of surface grain configurations [*Nickling*, 1988; *Li et al.*, 2008] and occurrence of turbulence-induced saltation bursts [*Carneiro et al.*, 2015].

Here, we use comprehensive high-frequency field measurements of aeolian transport at three field sites to determine which threshold(s) should be used in models for sand and dust flux. In Section 2, we present theory for predicting relationships among fluid and impact thresholds, wind speed fluctuations, and saltation transport occurrence. In Section 3, we describe methods for applying this theory to estimate thresholds from field data. In Section 4, we present the first field-based estimates of separate fluid and impact thresholds, and we examine how well these

thresholds predict measured saltation activities. In Section 5, we discuss how both thresholds control the occurrence of high-frequency variations in saltation activity, but how the impact threshold alone appears sufficient for model predictions of time-averaged (30-minute) sand and dust fluxes. We make concluding remarks in Section 6.

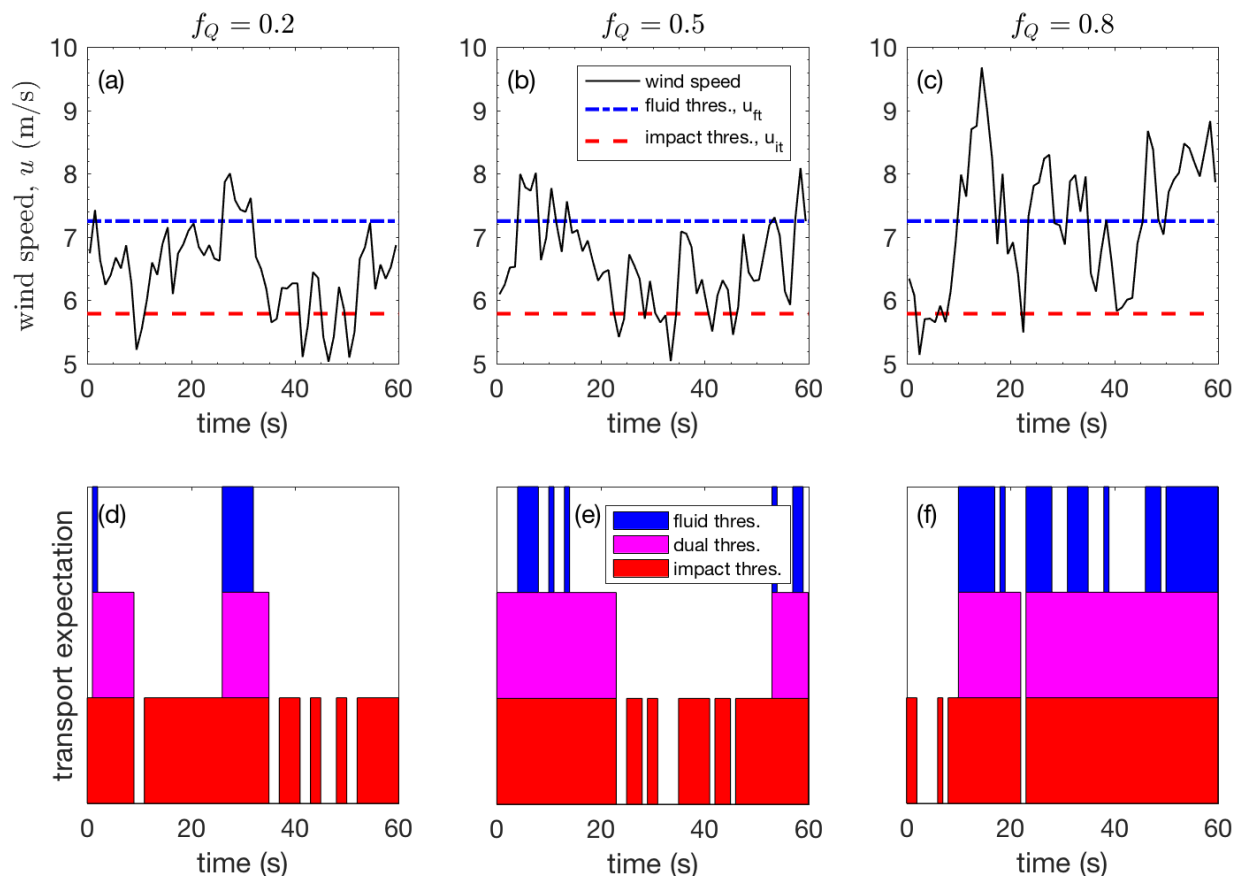


Figure 1. Illustration of variations in wind speed u for time intervals with (a) low ($f_Q = 0.2$, 16 May 2015, 15:04-15:05 local time), (b) medium ($f_Q = 0.5$, 18 May 2015, 16:42-16:43 local time), and (c) high ($f_Q = 0.8$, 27 May 2015, 16:38-16:39 local time) observed transport activity at Oceano. Blue and red dashed lines indicate respective fluid and impact threshold wind speeds, u_{ft} and u_{it} . (d-f) Expected instances of saltation occurrence for fluid threshold (Eq. 1 - blue), dual threshold (Eq. 3 - magenta), and impact threshold (Eq. 2 - red) control of saltation activity. Resulting activity predictions for respective fluid ($f_{Q,ft}$), dual ($f_{Q,dual}$), and impact ($f_{Q,it}$) threshold control are: (d) 0.12, 0.28, 0.82; (e) 0.15, 0.50, 0.85; and (f) 0.52, 0.82, 0.90.

2. Theory

We expect the occurrence of aeolian saltation transport to be governed by both the fluid and impact thresholds, based on the relative importance of transport initiation versus cessation. These combined contributions of τ_{ft} and τ_{it} should produce an intermediate “effective” threshold stress τ_{th} . In this section, we first describe how we expect τ_{ft} and τ_{it} to regulate saltation occurrence,

then we define a method for determining τ_{th} and hypothesize its relationship with f_Q , the fraction of time with active saltation.

2.1. Regulation of saltation occurrence by fluid and impact thresholds

Consider time series of near-surface horizontal wind speed $u(t)$ relative to fluid and impact threshold wind speeds, u_{ft} and u_{it} respectively, corresponding to τ_{ft} and τ_{it} (Fig. 1). When, $u \geq u_{ft}$, we unambiguously expect the occurrence of saltation transport; conversely, when $u < u_{it}$, transport should not occur. Ambiguity in prediction of saltation occurrence arises in cases where $u_{it} \leq u < u_{ft}$.

There are three possible ways to address this ambiguity. First, fluid threshold could dominate:

$$f_{Q,ft} = f_+, \quad (1)$$

where $f_{Q,ft}$ is the expected fraction of time with active saltation by fluid threshold control, and f_+ is the fraction of time with $u \geq u_{ft}$. Second, impact threshold could dominate:

$$f_{Q,it} = f_+ + f_-, \quad (2)$$

where $f_{Q,it}$ is the expected transport activity by impact threshold control, and f_- is the fraction of time with $u_{it} \leq u < u_{ft}$. Third, dual thresholds could together control saltation activity in a path-dependent manner [Kok, 2010b]:

$$f_{Q,dual} = f_+ + f_{\downarrow}f_-, \quad (3)$$

where $f_{Q,dual}$ is the expected transport activity for dual threshold control, and f_{\downarrow} is the fraction of time within $u_{it} \leq u < u_{ft}$ for which the most recent threshold crossing was a downward crossing of u_{ft} .

To illustrate these different threshold control scenarios, Figs. 1a-c display three sample time series of wind speed straddling fluid and impact thresholds, and Figs. 1d-f present predictions of the corresponding saltation activity by Eqs. 1-3. (Methods for obtaining $u(t)$, u_{ft} , and u_{it} will be described in further detail below.) These f_Q predictions differ due to different expectations for saltation occurrence during periods of ambiguous intermediate winds. In Fig. 1a, most intermediate winds originate from wind speeds below impact threshold and a state of expected non-transport (i.e., $f_{\downarrow} \rightarrow 0$); therefore, $f_{Q,dual} \rightarrow f_{Q,ft}$, indicating that fluid threshold mostly controls saltation occurrence (Fig. 1d). Conversely, in Fig. 1c, most intermediate winds originate from high wind speeds above impact threshold (i.e., $f_{\downarrow} \rightarrow 1$) and a state of expected transport; therefore, $f_{Q,dual} \rightarrow f_{Q,it}$, indicating that now impact threshold mostly controls saltation occurrence (Fig. 1f). In cases of intermediate winds approached from both directions (i.e., $f_{\downarrow} \approx 0.5$) and states of both non-transport and transport (Fig. 1b), $f_{Q,dual}$ is between $f_{Q,ft}$ and $f_{Q,it}$ (Fig. 1e).

2.2. “Effective” threshold in relation to dual thresholds and transport activity

To quantify the relative contributions of fluid and impact thresholds to the instantaneous occurrence of saltation, we adopt a statistical definition of “effective” threshold u_{th} based on the “Time Frequency Equivalence Method” [Stout and Zobeck, 1997; Stout, 2004; Wiggs et al., 2004]:

$$u_{th} = \Phi_u(1 - f_Q), \quad (4)$$

where $\Phi_u(1 - f_Q)$ is the value in the cumulative distribution of wind speeds Φ_u corresponding to the time fraction of inactive saltation, $1 - f_Q$. Thus, Eq. 4 asserts a statistical equivalence between the fraction of winds above u_{th} and the fraction of time with active saltation f_Q .

By the dual-threshold hypothesis (Eq. 3), both u_{it} and u_{ft} should contribute to f_Q , such that $u_{it} \leq u_{th} < u_{ft}$. Based on our reasoning for Fig. 1, we further hypothesize that cases of mostly inactive transport (i.e., $f_Q \approx 0$) should produce fluid threshold dominance (Eq. 1), whereas cases of mostly active transport (i.e. $f_Q \approx 1$) should produce impact threshold dominance (Eq. 2). Between these limiting cases, the effective threshold should vary with transport activity such that:

$$\tau_{th} = f_Q \tau_{it} + (1 - f_Q) \tau_{ft}, \quad (5)$$

where τ_{th} is the equivalent effective threshold shear stress for u_{th} . This phenomenon of decreasing τ_{th} with increasing wind speed (and presumably f_Q) was indeed observed in numerical simulations by Schönfeldt [2004]. If our depiction of effective threshold is correct, then Eq. 5 offers a way to estimate impact and fluid thresholds from measurements of effective threshold and saltation activity.

Below, in Section 3, we describe methods to estimate effective thresholds and saltation activities from field data. Then, in Section 4, we estimate impact and fluid thresholds from Eq. 5 and compare measured saltation activities against our hypotheses for saltation occurrence controlled by fluid (Eq. 1), impact (Eq. 2), and dual (Eq. 3) thresholds.

3. Methods

We analyzed simultaneous high-frequency measurements of active saltation and wind at three field sites (Jericoacoara, Rancho Guadalupe, and Oceano) with distinctive soil conditions. Multiple (3-9) Wenglor optical sensors [Barchyn *et al.*, 2014a] at heights from the bed surface up to ≈ 0.3 m counted saltating particles (25 Hz), which we converted to vertically-integrated saltation particle counts rates N (Fig. 2a). A sonic anemometer at height $z_U \approx 0.5$ m measured wind velocity (25 Hz at Jericoacoara and Rancho Guadalupe, 50 Hz at Oceano) (Fig. 2d). Full data collection methods are described in *Martin et al.* [2016].

To calculate saltation activity f_Q and effective threshold wind speed u_{th} , we applied $\delta t = 1$ s interval averaging to saltation (Fig. 2b) and wind (Fig. 2e) time series, then we subdivided these data into $\Delta t = 1$ minute analysis intervals. Within each analysis interval, we calculated saltation activity f_Q as the fraction of δt increments within Δt for which N was nonzero (Fig 2c) and applied a correction (see Supporting Information Text S1) to account for the possibility of false negatives. For each Δt , we then obtained corresponding wind speed distributions Φ_u for the δt -averaged u values, and we used f_Q and Φ_u to calculate u_{th} by Eq. 4 (Fig. 2f). We chose the averaging interval $\delta t = 1$ s based on the typical response time of saltation to turbulent wind fluctuations [e.g., *Anderson and Haff*, 1988; *McEwan and Willetts*, 1991; *Ma and Zheng*, 2011], and we chose the analysis interval to represent the typical oscillation period for large-scale structures in an atmospheric boundary layer [e.g., *Guala et al.*, 2011]. We further justify our time scale choices in Supporting Information Text S2.

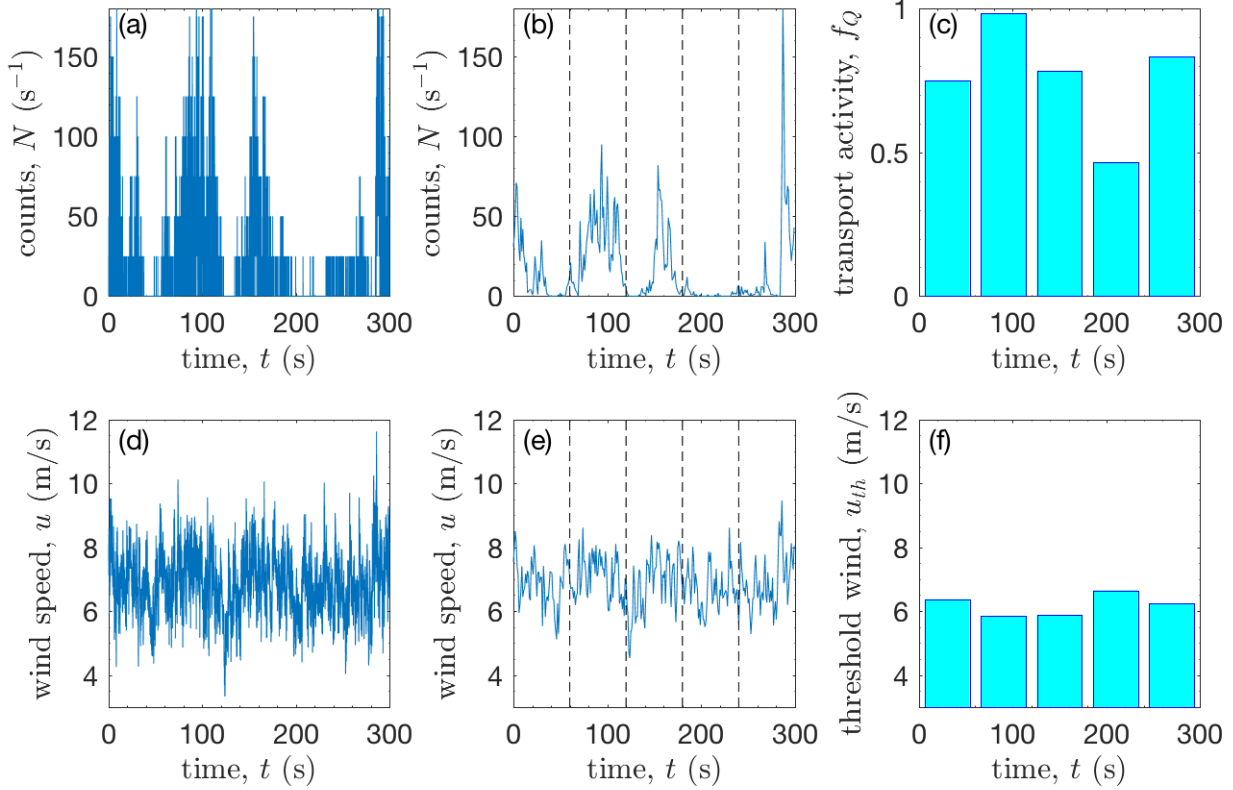


Figure 2. Illustration of method to calculate transport activity f_Q and effective threshold wind speed u_{th} from high-frequency sand flux and wind speed measurements. (a) Sample time series of total particle counts N , from deployment at Rancho Guadalupe (24 March 2015, 13:31-13:36 local time). (b) $\delta t = 1$ s interval-averaged N time series. Vertical dashed lines indicate $\Delta t = 1$ minute analysis intervals. (c) Transport activities f_Q , calculated as fraction of δt increments in each Δt for which $N > 0$, and corrected for false negatives (Supporting Information Text S1). (d) Sample time series of streamwise wind speed u . (e) $\delta t = 1$ s interval-averaged u . Vertical dashed lines again indicate Δt . (f) Resulting values of threshold wind speed u_{th} calculated by Eq. 4 from corresponding f_Q and wind speed distributions Φ_u for each Δt .

We converted effective threshold wind speeds u_{th} to effective threshold shear velocities $u_{*,th}$ and stresses τ_{th} by the law-of-the-wall and the standard τ - u_* relationship:

$$u_{th} = \frac{u_{*,th}}{\kappa} \ln\left(\frac{z_U}{z_0}\right), \quad (6)$$

$$\tau_{th} = \rho_f u_{*,th}^2. \quad (7)$$

To justify use of the law-of-the-wall, which only applies to neutrally-stable conditions, we limited our analyses to those intervals with stability parameter $|z/L| \leq 0.2$, below which law-of-the-wall and Reynolds stress estimates of shear stress are roughly equivalent [Salesky *et al.*, 2012]. In addition, we analyzed only those intervals with wind direction aligned with prevailing sediment-transporting winds, i.e. $|\theta| \leq 20^\circ$. We applied Eqs. 6-7 to values of u_{th} grouped into f_Q bins, facilitating calculation of standard errors for u_{th} and propagation of this uncertainty into calculations of $u_{*,th}$ and τ_{th} (see Supporting Information Text S3). We set the air density ρ_f in Eq. 7 based on the mean temperature at each site [Martin *et al.*, 2016], and we assumed the

standard von Karman parameter $\kappa \approx 0.4$ in Eq. 6. We calculated aerodynamic roughness heights z_0 in Eq. 6 for each site based on wind velocity profiles for zero transport, and we found statistically insignificant changes in “effective” roughness z_s with transport activity (Supporting Information Text S4). Thus, we assume that known systematic increase in z_s [e.g., *Sherman*, 1992] and possible decrease in κ_s [*Li et al.*, 2010] with saltation intensity do not bias our calculations for Eq. 6.

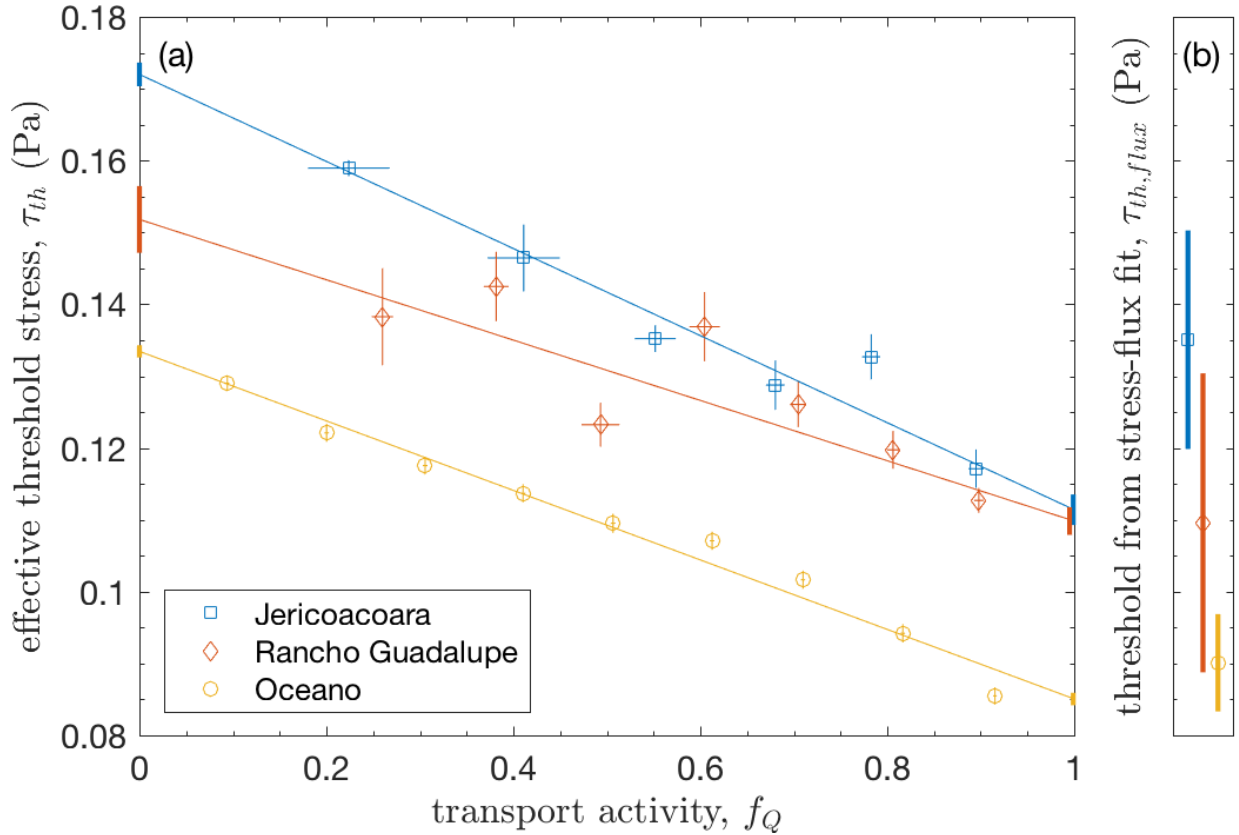


Figure 3. (a) Effective threshold stress τ_{th} versus transport activity f_Q . Error bars correspond to 1 standard error for binned values. Color-coded lines show least-squares fit to Eq. 5 at each field site. Vertical bars at $f_Q = 0$ provide estimates for fluid threshold τ_{ft} and its uncertainty from the linear fit; bars at $f_Q = 1$ are for impact threshold. (b) Thresholds estimated by *Martin and Kok* [2016] from zero-intercept of fit to saltation flux versus shear stress $\tau_{th,flux}$. Specific values for τ_{ft} , τ_{it} , and $\tau_{th,flux}$ are listed in Supporting Information Table S1.

4. Results

We use the methods described in Section 3 to calculate effective threshold stresses and saltation activities at our three field sites, which we then use to estimate fluid and impact threshold stresses and evaluate our hypotheses on dual threshold control of saltation activity described in Section 2.

As predicted by Eq. 5, we find that the effective threshold stress τ_{th} decreases linearly with saltation activity f_Q at each of the field sites (Fig. 3a). Based on Eq. 5, we calculate fluid and impact threshold stresses, τ_{ft} and τ_{it} , from the limiting effective threshold values for no transport ($f_Q \rightarrow 0$) and continuous transport ($f_Q \rightarrow 1$), as shown in Fig. 3a. Converting fluid and impact threshold stresses to threshold shear velocities by Eq. 6, we calculate threshold ratios $u_{*,it}/u_{*,ft} = 0.805 \pm 0.013$, 0.851 ± 0.021 , and 0.798 ± 0.008 at Jericoacoara, Rancho Guadalupe, and Oceano, respectively, which are consistent with laboratory measurements [Bagnold, 1937] and numerical predictions [Kok, 2010a] of $u_{*,it}/u_{*,ft} \approx 0.8$.

To more thoroughly test our theory describing the relative influence of fluid and impact thresholds on saltation activity, we compare measured saltation activities f_Q to those expected for fluid ($f_{Q,ft}$), impact ($f_{Q,it}$), and dual ($f_{Q,dual}$) threshold control of saltation occurrence. We predict these expected transport activities by applying Eqs. 1-3 to measured fluctuations in wind time series $u(t)$, relative to fluid and impact threshold wind speeds calculated from τ_{ft} and τ_{it} by Eqs. 6 and 7 (Fig. 1). As expected, dual threshold control provides the best explanation for the observed transport activity at all sites, while fluid and impact threshold control respectively under- and over-predict transport activity (Fig. 4; see Supporting Information Text S6 for description of chi-square tests for Eqs. 1-3 predictions.) Also as expected, $f_{Q,ft}$ approaches $f_{Q,dual}$ near the limit of no transport ($f_Q \rightarrow 0$); conversely, $f_{Q,it}$ approaches $f_{Q,dual}$ in the limit of continuous transport ($f_Q \rightarrow 1$). Despite the fact that dual threshold control somewhat overpredicts and underpredicts saltation activity during respective low and high observed saltation activity at Oceano (Fig. 4c), these observations otherwise generally confirm our prediction that dual thresholds provide the best explanation for transport activity, but that fluid and impact thresholds alone are sufficient to explain the limiting cases of negligible and continuous saltation transport.

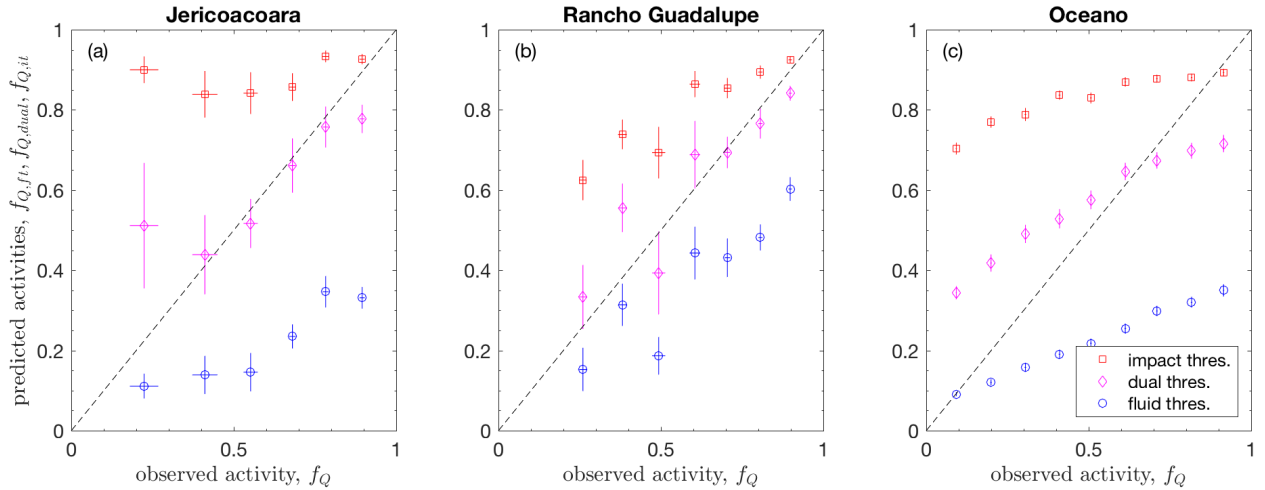


Figure 4. Predicted transport activities versus observed transport activities f_Q for impact threshold control $f_{Q,it}$ (Eq. 2), dual threshold control $f_{Q,dual}$ (Eq. 3), and fluid threshold control $f_{Q,ft}$ (Eq. 1). Observations for (a) Jericoacoara, (b) Rancho Guadalupe, and (c) Oceano.

5. Discussion

Our results provide the first field-based evidence for the occurrence of separate fluid and impact thresholds in aeolian saltation. Though fluid and impact thresholds for saltation initiation and cessation have long been theorized [e.g., *Bagnold*, 1937; *Kok*, 2010b] and measured in wind tunnel experiments [e.g., *Iversen and Rasmussen*, 1994], the difficulty of directly measuring threshold crossings in the field [e.g., *Barchyn and Hugenholtz*, 2011] has limited the ability of past studies to resolve both thresholds. To overcome these limitations, we considered how dual thresholds together control the occurrence of saltation transport (Eqs. 1-3), such that the statistically-defined effective threshold [*Stout and Zobeck*, 1997; *Stout*, 2004] combines contributions of fluid and impact thresholds weighted by the observed saltation activity (Eq. 5). By fitting observed saltation activities and effective thresholds to Eq. 5, we calculated distinct fluid and impact threshold stresses at three field sites (Fig. 3). Then, we showed how wind fluctuations around these dual thresholds mostly explain observed saltation activities, except in limiting cases of infrequent ($f_Q \rightarrow 0$) or near-continuous ($f_Q \rightarrow 1$) transport, for which the respective fluid or impact thresholds alone provide sufficient predictive power (Fig. 4).

Though our analysis is strongly supportive of the existence of separate fluid and impact thresholds that together control saltation activity, it does have two potential limitations. First, the threshold stresses and shear velocities we computed at each site are potentially sensitive to the specific averaging interval δt and analysis interval Δt we applied to our calculations (Fig. 2) [*Stout*, 1998; *Wiggs et al.*, 2004; *Barchyn and Hugenholtz*, 2011]. However, for a range of δt around the saltation response time of 1s [e.g., *Anderson and Haff*, 1988; *McEwan and Willetts*, 1991; *Ma and Zheng*, 2011] and a wide range of Δt , we observed only small variations in τ_{it} , τ_{ft} , and u_{*it}/u_{*ft} that remain broadly consistent with independent measurements [*Bagnold*, 1937; *Kok*, 2010b] (Supporting Information Text S2). Second, observed threshold trends may in fact be controlled by diurnal variation in atmospheric stability [e.g., *Frank and Kocurek*, 1994] or broader secular changes in soil properties [e.g., *Greeley and Iversen*, 1985] not accounted for by our analysis. To assess this, we compared τ_{th} values obtained at different times and on different days at Oceano, which revealed no systematic diurnal variation and only slight secular variation in effective threshold and inferred fluid and impact thresholds (Supporting Information Text S7). We note that our observed values for τ_{ft} and τ_{it} are significantly larger than expected by wind tunnel-derived fluid [*Greeley and Iversen*, 1985; *Shao and Lu*, 2000; Eq. 2.5 in *Kok et al.*, 2012] and impact [*Kok et al.*, 2012; Eq. S1 in *Lapotre et al.*, 2016] threshold predictions for the median soil particle diameters at our sites, and that future work is needed to understand how properties of the granular bed contribute to threshold values at specific sites.

Recent wind tunnel measurements of bed surface shear stress τ_0 versus saltation flux Q [*Walter et al.*, 2014] support our interpretations of how fluid and impact thresholds govern saltation transport. *Walter et al.* found that, so long as saltation activity is continuous (i.e., $f_Q = 1$), τ_0 remains constant with changes in Q . By *Owen's* hypothesis [*Owen*, 1964], *Walter et al.* interpreted this constant τ_0 as implying a constant rate of wind momentum dissipation at the bed surface equal to the impact threshold stress τ_{it} . However, they also observed τ_0 to decrease monotonically from τ_{ft} to τ_{it} during the transition from no saltation to continuous saltation [Fig. 4 in *Walter et al.*, 2014]. This result implies that τ_0 , like effective threshold τ_{th} , is governed by changes in f_Q modulating the relative importance of fluid and impact thresholds, as in Eq. 5.

The role of fluid and impact thresholds in determining saltation activity f_Q (Eq. 3), effective threshold τ_{th} (Eq. 5), and possibly also the rate of momentum dissipation τ_0 [Walter *et al.*, 2014], offers insight into which threshold(s) should be used in saltation flux modeling. By calculating the zero-intercept of the linear fit to saltation flux Q versus shear stress τ , Martin and Kok [2016] calculated “flux-based” threshold stresses $\tau_{th,flux}$, which they interpreted as τ_0 in the saltation momentum balance [e.g., Kok *et al.*, 2012]. Notably, at all sites except Jericoacoara, these values for $\tau_{th,flux}$ agree with our τ_{it} measurements within uncertainty ranges (Fig. 3), and in all cases $\tau_{th,flux}$ values are closer to τ_{it} than to τ_{ft} . This agreement implies that, as in Walter *et al.* [2014], τ_{it} primarily determines the rate of momentum dissipation in saltation flux modeling. Due to the relatively small difference between τ_{it} and τ_{ft} on Earth, wind speed distributions for time-averaged shear stresses greater than τ_{it} contain many instances of stress temporarily exceeding τ_{ft} and therefore initiating saltation [Kok, 2010a], so that fluid threshold will not significantly contribute to $\tau_{th,flux}$. Therefore, τ_{it} alone can serve as the *de facto* threshold for saltation in comparisons of saltation flux and shear stress measured over longer time intervals (i.e., 30 minutes), while τ_{ft} may merely serve as a rough boundary between intermittent and continuous saltation (Supporting Information Fig. S8). However, when the gap between fluid and impact thresholds is larger, as on Mars [Kok, 2010b] and several other planetary bodies [Pächtz and Durán, 2016], τ_{ft} may need to be included in saltation flux models.

These findings offer insight into how the threshold should be incorporated into models for sand and dust flux. Dual thresholds should be considered together for predictions of high-frequency saltation fluctuations [e.g., Li *et al.*, 2014] or for modeling of saltation on Mars [Kok, 2010b] or other planetary bodies [Pächtz and Durán, 2016] where the separation between fluid and impact thresholds is much larger than on Earth. However, when modeling saltation flux over longer averaging times (i.e., 30 minutes), such as in large-scale models for wind erosion [e.g., Chepil, 1945], dune migration [e.g., Fryberger *et al.*, 1979], and dust emission [e.g., Gillette and Passi, 1988], our results indicate that use of the impact threshold alone is sufficient.

6. Conclusion

Here we offered the first field-based evidence of distinct fluid and impact thresholds for the respective initiation and cessation of aeolian saltation. The measured ratio of these thresholds is consistent with past laboratory and numerical studies of dual thresholds. The presence of two distinct thresholds causes high-frequency (~ 1 min) fluctuations in transport activity to be controlled by both the fluid and impact thresholds. When saltation is active a small fraction of the time, fluid threshold dominates. As saltation activity increases, so too does the relative contribution of impact threshold, until it dominates under near-continuous transport conditions. However, our results indicate that the impact threshold alone is sufficient for explaining the time-averaged (~ 30 mins) momentum dissipation during terrestrial saltation and therefore the zero-intercept of saltation flux laws. Consequently, parameterizations of sand and dust transport in models, which currently predominantly use the fluid threshold, should instead use the impact threshold.

ACKNOWLEDGEMENTS. U.S. National Science Foundation (NSF) Postdoctoral Fellowship EAR-1249918 to R.L.M., NSF grant AGS-1358621 to J.F.K., and ARO grant W911NF-15-1-0417 to J.F.K. supported this research. Oceano Dunes State Vehicular Recreation Area, Rancho Guadalupe Dunes Preserve, and Jericoacoara National Park provided essential site access and support. We thank Marcelo Chamecki for advice on treatment of wind data, Chris Hugenholtz and Tom Barchyn for equipment help, Doug Jerolmack for lab access for grain-size analysis, and Jean Ellis, Paulo Sousa, Peter Li, Francis Turney, Arkayan Samaddar, and Livia Freire for field assistance.

References

- Anderson, R. S., and P. K. Haff (1988), Simulation of eolian saltation, *Science*, *241*(4867), 820–823, doi:10.1126/science.241.4867.820.
- Ayoub, F., J.-P. Avouac, C. E. Newman, M. I. Richardson, A. Lucas, S. Leprince, and N. T. Bridges (2014), Threshold for sand mobility on Mars calibrated from seasonal variations of sand flux, *Nat. Commun.*, *5*, 5096.
- Baas, A. C. W. (2008), Challenges in aeolian geomorphology: Investigating aeolian streamers, *Geomorphology*, *93*(1–2), 3–16, doi:10.1016/j.geomorph.2006.12.015.
- Bagnold, R. A. (1937), The transport of sand by wind, *Geogr. J.*, *89*(5), 409–438, doi:10.2307/1786411.
- Bagnold, R. A. (1941), *The Physics of Blown Sand and Desert Dunes*, Dover, London.
- Barchyn, T. E., and C. H. Hugenholtz (2011), Comparison of four methods to calculate aeolian sediment transport threshold from field data: Implications for transport prediction and discussion of method evolution, *Geomorphology*, *129*(3–4), 190–203, doi:10.1016/j.geomorph.2011.01.022.
- Barchyn, T. E., C. H. Hugenholtz, B. Li, C. McKenna Neuman, and R. S. Sanderson (2014a), From particle counts to flux: Wind tunnel testing and calibration of the “Wenglor” aeolian sediment transport sensor, *Aeolian Res.*, *15*, 311–318, doi:10.1016/j.aeolia.2014.06.009.
- Barchyn, T. E., R. L. Martin, J. F. Kok, and C. H. Hugenholtz (2014b), Fundamental mismatches between measurements and models in aeolian sediment transport prediction: The role of small-scale variability, *Aeolian Res.*, *15*, 245–251, doi:10.1016/j.aeolia.2014.07.002.
- Bevington, P. R., and D. K. Robinson (2003), *Data reduction and error analysis for the physical sciences*, 3rd ed., McGraw-Hill, New York.
- van Boxel, J. H., G. Sterk, and S. M. Arens (2004), Sonic anemometers in aeolian sediment transport research, *Geomorphology*, *59*(1–4), 131–147, doi:10.1016/j.geomorph.2003.09.011.
- Bridges, N. T., F. Ayoub, J.-P. Avouac, S. Leprince, A. Lucas, and S. Mattson (2012), Earth-like sand fluxes on Mars, *Nature*, *485*(7398), 339–342, doi:10.1038/nature11022.
- Carneiro, M. V., K. R. Rasmussen, and H. J. Herrmann (2015), Bursts in discontinuous Aeolian saltation, *Sci. Rep.*, *5*, doi:10.1038/srep11109.
- Chepil, W. S. (1945), Dynamics of Wind Erosion. 2. Initiation of soil movement, *Soil Sci.*, *60*(5), 397, doi:10.1097/00010694-194511000-00005.
- Creysseels, M., P. Dupont, A. O. El Moctar, A. Valance, I. Cantat, J. T. Jenkins, J. M. Pasini, and K. R. Rasmussen (2009), Saltating particles in a turbulent boundary layer: Experiment and theory, *J. Fluid Mech.*, *625*, 47–74, doi:10.1017/S0022112008005491.
- Davidson-Arnott, R. G. D., and B. O. Bauer (2009), Aeolian sediment transport on a beach: Thresholds, intermittency, and high frequency variability, *Geomorphology*, *105*(1–2), 117–126, doi:10.1016/j.geomorph.2008.02.018.
- Davidson-Arnott, R. G. D., K. MacQuarrie, and T. Aagaard (2005), The effect of wind gusts, moisture content and fetch length on sand transport on a beach, *Geomorphology*, *68*(1–2), 115–129, doi:10.1016/j.geomorph.2004.04.008.

- Frank, A., and G. Kocurek (1994), Effects of atmospheric conditions on wind profiles and aeolian sand transport with an example from White Sands National Monument, *Earth Surf. Process. Landf.*, 19(8), 735–745, doi:10.1002/esp.3290190806.
- Fryberger, S. G., G. Dean, and E. D. McKee (1979), Dune forms and wind regime, in *A Study of Global Sand Seas, U.S. Geological Survey Professional Paper, 1052*, pp. 137–170.
- Gillette, D. A., and R. Passi (1988), Modeling dust emission caused by wind erosion, *J. Geophys. Res. Atmospheres*, 93(D11), 14233–14242, doi:10.1029/JD093iD11p14233.
- Greeley, R., and J. D. Iversen (1985), *Wind as a Geological Process on Earth, Mars, Venus and Titan*, Cambridge University Press, New York.
- Guala, M., M. Metzger, and B. J. McKeon (2011), Interactions within the turbulent boundary layer at high Reynolds number, *J. Fluid Mech.*, 666, 573–604, doi:10.1017/S0022112010004544.
- Iversen, J. D., and K. R. Rasmussen (1994), The effect of surface slope on saltation threshold, *Sedimentology*, 41(4), 721–728, doi:10.1111/j.1365-3091.1994.tb01419.x.
- Iversen, J. D., and B. R. White (1982), Saltation threshold on Earth, Mars and Venus, *Sedimentology*, 29(1), 111–119, doi:10.1111/j.1365-3091.1982.tb01713.x.
- Kok, J. F. (2010a), An improved parameterization of wind-blown sand flux on Mars that includes the effect of hysteresis, *Geophys. Res. Lett.*, 37(12), L12202, doi:10.1029/2010GL043646.
- Kok, J. F. (2010b), Difference in the wind speeds required for initiation versus continuation of sand transport on Mars: Implications for dunes and dust storms, *Phys. Rev. Lett.*, 104(7), 74502, doi:10.1103/PhysRevLett.104.074502.
- Kok, J. F., E. J. R. Parteli, T. I. Michaels, and D. B. Karam (2012), The physics of wind-blown sand and dust, *Rep. Prog. Phys.*, 75, 106901, doi:10.1088/0034-4885/75/10/106901.
- Kok, J. F. et al. (2014), An improved dust emission model – Part 1: Model description and comparison against measurements, *Atmos Chem Phys*, 14(23), 13023–13041, doi:10.5194/acp-14-13023-2014.
- Lapotre, M. G. A. et al. (2016), Large wind ripples on Mars: A record of atmospheric evolution, *Science*, 353(6294), 55–58, doi:10.1126/science.aaf3206.
- Li, B., D. J. Sherman, E. J. Farrell, and J. T. Ellis (2010), Variability of the apparent von Karman parameter during aeolian saltation, *Geophys. Res. Lett.*, 37(15), L15404, doi:10.1029/2010GL044068.
- Li, B., J. T. Ellis, and D. J. Sherman (2014), Estimating the impact threshold for wind-blown sand, *J. Coast. Res.*, 627–632, doi:10.2112/SI70-106.1.
- Li, Z., X. Zhao, and W. Huang (2008), A stochastic model for initial movement of sand grains by wind, *Earth Surf. Process. Landf.*, 33(11), 1796–1803, doi:10.1002/esp.1638.
- Lindhorst, S., and C. Betzler (2016), The climate-archive dune: Sedimentary record of annual wind intensity, *Geology*, 44(9), 711–714, doi:10.1130/G38093.1.
- Lorenz, R. D., and J. R. Zimbelman (2014), *Dune Worlds*, Springer, Heidelberg.
- Ma, G. S., and X. J. Zheng (2011), The fluctuation property of blown sand particles and the wind-sand flow evolution studied by numerical method, *Eur. Phys. J. E*, 34(5), doi:10.1140/epje/i2011-11054-3.
- Martcorena, B., and G. Bergametti (1995), Modeling the atmospheric dust cycle: 1. Design of a soil-derived dust emission scheme, *J. Geophys. Res. Atmospheres*, 100(D8), 16415–16430, doi:10.1029/95JD00690.

- Martin, R. L., and J. F. Kok (2016), Linear scaling of wind-driven sand flux with shear stress, *arXiv:1609.09458v2*.
- Martin, R. L., J. F. Kok, and M. Chamecki (2016), High-frequency field observations of aeolian saltation interactions with turbulent boundary layer winds, *arXiv:1609.08707v1*.
- McEwan, I. K., and B. B. Willetts (1991), Numerical model of the saltation cloud., *Acta Mech. Suppl*, 1, 53–66.
- Nickling, W. G. (1988), The initiation of particle movement by wind, *Sedimentology*, 35(3), 499–511, doi:10.1111/j.1365-3091.1988.tb01000.x.
- Owen, P. R. (1964), Saltation of uniform grains in air, *J. Fluid Mech.*, 20(2), 225–242, doi:10.1017/S0022112064001173.
- Pächtz, T., and O. Durán (2016), Fluid forces or impacts, what governs the entrainment of soil particles in sediment transport mediated by a Newtonian fluid?, *arXiv:1605.07306v3*.
- Rice, M. A., I. K. McEwan, and C. E. Mullins (1999), A conceptual model of wind erosion of soil surfaces by saltating particles, *Earth Surf. Process. Landf.*, 24(5), 383–392, doi:10.1002/(SICI)1096-9837(199905)24:5<383::AID-ESP995>3.0.CO;2-K.
- Salesky, S. T., M. Chamecki, and N. L. Dias (2012), Estimating the random error in eddy-covariance based fluxes and other turbulence statistics: the filtering method, *Bound.-Layer Meteorol.*, 144(1), 113–135, doi:10.1007/s10546-012-9710-0.
- Schönfeldt, H. J. (2004), Establishing the threshold for intermittent aeolian sediment transport., *Meteorol. Z.*, 13(5), 437–444, doi:10.1127/0941-2948/2004/0013-0437.
- Shao, Y., and H. Lu (2000), A simple expression for wind erosion threshold friction velocity, *J. Geophys. Res.*, 105(D17), 22437–22443, doi:200010.1029/2000JD900304.
- Sherman, D. J. (1992), An equilibrium relationship for shear velocity and apparent roughness length in aeolian saltation, *Geomorphology*, 5(3–5), 419–431, doi:10.1016/0169-555X(92)90016-H.
- Sherman, D. J., B. Li, J. T. Ellis, E. J. Farrell, L. P. Maia, and H. Granja (2013), Recalibrating aeolian sand transport models, *Earth Surf. Process. Landf.*, 38(2), 169–178, doi:10.1002/esp.3310.
- Stout, J. E. (1998), Effect of averaging time on the apparent threshold for aeolian transport, *J. Arid Environ.*, 39(3), 395–401, doi:10.1006/jare.1997.0370.
- Stout, J. E. (2004), A method for establishing the critical threshold for aeolian transport in the field, *Earth Surf. Process. Landf.*, 29(10), 1195–1207, doi:10.1002/esp.1079.
- Stout, J. E., and T. M. Zobeck (1997), Intermittent saltation, *Sedimentology*, 44(5), 959–970, doi:10.1046/j.1365-3091.1997.d01-55.x.
- Ungar, J. E., and P. K. Haff (1987), Steady state saltation in air, *Sedimentology*, 34(2), 289–299, doi:10.1111/j.1365-3091.1987.tb00778.x.
- Walter, B., S. Horender, C. Voegeli, and M. Lehning (2014), Experimental assessment of Owen’s second hypothesis on surface shear stress induced by a fluid during sediment saltation, *Geophys. Res. Lett.*, 41(17), 6298–6305, doi:10.1002/2014GL061069.
- Webb, N. P., M. S. Galloza, T. M. Zobeck, and J. E. Herrick (2016), Threshold wind velocity dynamics as a driver of aeolian sediment mass flux, *Aeolian Res.*, 20, 45–58.

Wiggs, G. F. S., R. J. Atherton, and A. J. Baird (2004), Thresholds of aeolian sand transport: establishing suitable values, *Sedimentology*, 51(1), 95–108, doi:10.1046/j.1365-3091.2003.00613.x.

Supporting Information for

Field measurements demonstrate distinct initiation and cessation thresholds governing aeolian sediment transport flux

Raleigh L. Martin¹ and Jasper F. Kok¹

¹Department of Atmospheric and Oceanic Sciences, University of California, Los Angeles, CA 90095

Contents of this file

Text S1 to S8
Figures S1 to S8
Tables S1 to S5

Introduction

In this supporting document, we describe details associated with the analyses presented in the main paper. Text S1 describes a correction to account for false negatives when calculating saltation activity, Text S2 justifies our choices of averaging and analysis intervals, Text S3 explains methods for calculating and propagating uncertainty in threshold estimates, Text S4 presents calculations for the roughness height used to convert wind speed to shear stress, Text S5 details methods for computing fluid and impact thresholds, Text S6 compares statistical tests for viability of different threshold models, Text S7 considers the possibility of diurnal or secular trends affecting threshold variability, and Text S8 lists variables used in the main paper and Supporting Information Text. Supporting Figures (S1-S8) and Tables (S1-S5) accompany this text.

Text S1. Accounting for false negatives in calculation of saltation activity

Here, we derive a method to account for the possibility of “false negatives” (i.e., instances in which saltation transport occurs but is not detected) when computing saltation activity f_Q . To do so, we distinguish the measured saltation detection rate f_D from the actual saltation activity f_Q . We compute f_D as the fraction of averaging intervals δt in each analysis interval Δt for which total particle counts rate N is nonzero. We then estimate f_Q from f_D by calculating the expected rate of false negatives for particle arrivals occurring as a Poisson counting process. We detail this procedure below.

By Bayes Theorem, we have:

$$f_{D|Q} = \frac{f_D f_{Q|D}}{f_Q}, \quad (\text{S1})$$

where $f_{D|Q}$ is the conditional probability of detecting transport when it is active, and $f_{Q|D}$ is the probability that transport is actually active when it has been detected. We observed that the Wenglor optical particle counters did not produce “false positives,” i.e. that detection necessarily implied transport and therefore that $f_{Q|D} = 1$. However, we found that during conditions of weak transport or few Wenglor counters, false negatives could occur with some regularity due to the limited sampling volume of individual counters. Denoting these false negatives as $f_{\sim D|Q}$ and noting that $f_{\sim D|Q} + f_{D|Q} = 1$, we can restate Eq. S1 as:

$$f_Q = \frac{f_D}{1 - f_{\sim D|Q}}. \quad (\text{S2})$$

To estimate the rate of false negatives $f_{\sim D|Q}$, we treat particle arrivals as a Poisson counting process. For such a process:

$$f_{\sim D|Q} = \exp(-\lambda), \quad (\text{S3})$$

where λ is the average arrival rate of particles per δt averaging interval at times when transport is active. We calculate λ as:

$$\lambda = \bar{N} \delta t / f_D, \quad (\text{S4})$$

where \bar{N} is the mean particle counts rate during the analysis interval $\Delta t = 1$ minute. Combining Eqs. S2-S4, we have:

$$f_Q = \frac{f_D}{1 - \exp(-\lambda)} = \frac{f_D}{1 - \exp(-\bar{N} \delta t / f_D)}. \quad (\text{S5})$$

The effect of the false negative correction in computing f_Q can be seen in Fig. S1. During strong transport, λ is large so $f_Q \approx f_D$ in Eq. S5. However, when transport is weak, δt is small, or the number of Wenglors are few, λ can be much smaller than 1, and therefore the correction causes f_Q to significantly exceed f_D .

Text S2. Selection and justification of averaging and analysis time intervals for calculations of saltation activity and effective threshold

Recognizing that calculations of saltation activity f_Q and effective threshold wind speed u_{th} are sensitive to averaging interval δt and analysis interval Δt [Stout, 1998; Barchyn and Hugenholtz, 2011], here we provide physical explanations for our selection of these values, then we perform analyses to investigate the sensitivity of our results to the choice of these time scales and to justify these choices.

S2.1. Physical basis for selecting averaging and analysis intervals

Noting the possible sensitivity of u_{th} calculations to selection of δt and Δt , we chose these averaging and analysis timescales through consideration of saltation transport mechanics and the requirements of the statistical analysis. For averaging interval, we chose the conventional $\delta t = 1$ s [e.g., Stout and Zobeck, 1997] based on the typical response time of saltation to turbulent wind fluctuations [e.g., Anderson and Haff, 1988; McEwan and Willetts, 1991; Ma and Zheng, 2011]. For the analysis interval Δt , we require a timescale that is much larger than seconds, because of the decoupling of spatially-separated wind and saltation time series over such short timescales [e.g., Baas, 2008]. Because the typical oscillation of large-scale structures in an atmospheric boundary layer is roughly 1 minute [e.g., Guala et al., 2011], Φ_u and f_Q determined at or above this timescale should provide representative statistical snapshots of wind and saltation fluctuations. Therefore, we chose $\Delta t = 1$ minute to satisfy these statistical sampling requirements while maximizing the number of analysis windows.

S2.2. Sensitivity analysis for effect of averaging interval

To examine the effect of averaging interval δt on the relation between f_Q and u_{th} , we redo the analysis from Fig. 3a for five values of δt : 0.5 s, 0.72 s, 1 s, 1.4 s, and 2 s. The resulting plots for Oceano, where the data are most voluminous, are shown in Fig. S2. The computed limiting values of fluid threshold τ_{ft} , impact threshold τ_{it} , and threshold ratio $u_{*,it}/u_{*,ft}$, are provided in Table S2.

There are two effects of averaging interval δt . First, the probability of detecting particles in each averaging interval increases with δt . This “flux detection effect” increases f_Q with increasing δt , and therefore it decreases u_{th} by Eq. 4. Second, by averaging over extreme events, the distribution of wind speeds Φ_u narrows with increasing δt . For small f_Q , this “wind distribution effect” will decrease u_{th} with increasing δt ; for large f_Q , it will increase u_{th} with increasing δt .

The outcome of these two effects can be seen in Fig. S2. The fluid threshold τ_{ft} , which corresponds to the lower limit $f_Q \rightarrow 0$, displays a substantial decrease in τ_{th} with increasing δt by a combination of the flux detection effect and wind distribution effect. In contrast, the impact threshold τ_{it} , which corresponds to the upper limit $f_Q \rightarrow 1$, shows a minor increase in τ_{th} with increasing δt , as the increase from the wind distribution effect slightly outweighs the decrease by the flux detection effect. The combined result of decreasing τ_{ft} and increasing τ_{it} is to increase the threshold ratio $u_{*,it}/u_{*,ft}$ with increasing δt (Table S2).

S2.3. Sensitivity analysis for effect of analysis interval

Our choice of $\Delta t = 1$ minute was somewhat arbitrary: long enough to produce statistically-representative values for each analysis interval but short enough to generate a wide range of data points for analysis. In particular, making Δt much larger than 1 minute would have eliminated our ability to evaluate the full range of saltation activities at Jericoacoara and Rancho Guadalupe.

At Oceano, where the data are significantly more extensive, we are able to perform a sensitivity analysis to evaluate the effect of varying the analysis interval from 0.5 to 10 minutes. Holding averaging interval δt constant at 1 s, we consider 5 values for Δt at Oceano: 0.5 minutes, 1 minute, 2 minutes, 5 minutes, and 10 minutes. The resulting calculations of τ_{th} versus f_Q are shown in Fig. S3. The computed limiting values of fluid threshold τ_{ft} , impact threshold τ_{it} , and threshold ratio $u_{*,it}/u_{*,ft}$, are provided in Table S3. In all cases, the effect of changing Δt is negligible.

Text S3. Estimation of uncertainties for effective threshold wind speeds, shear velocities, and shear stresses

To facilitate uncertainty estimation for computed effective thresholds, we combined effective threshold wind speed values u_{th} from individual Δt analysis intervals into bins defined by ranges of flux activity f_Q . For each bin, we computed bin-averaged threshold and activity values for u_{th} and f_Q , then we calculated their uncertainties from the standard errors of values in each bin. When converting each bin-averaged effective threshold wind speed u_{th} to an effective threshold shear velocity $u_{*,th}$ and shear stress τ_{th} , we performed error propagation to estimate uncertainties in $u_{*,th}$ and τ_{th} .

S3.1. Creation of flux activity bins

For each site, we grouped values of u_{th} for individual Δt together into bins covering ranges of f_Q . To accommodate the uneven spread of data points across the range of possible f_Q , we allowed for creation of bins covering varying ranges of f_Q . These criteria were established to balance the need for a sufficient number of data points in each bin but to limit the maximum width of the bins. The procedure for generating the binned values for each site is as follows:

- (1) Sort all u_{th} data points in order of increasing f_Q . Because the effective threshold calculation (Eq. 1) assumes intermittent transport conditions, exclude data points with $f_Q < 0.05$ and $f_Q > 0.95$.
- (2) Starting from the lowest remaining f_Q , add data points to the bin, until the following criteria are achieved for the bin
 - a. $\max(f_Q) - \min(f_Q) \geq 0.1$ (minimum bin width), AND
 - b. There are at least 3 points in the bin OR $\max(f_Q) - \min(f_Q) > 0.2$ (maximum bin width).
- (3) Once the bin is full, repeat step 2 for the next bin.

S3.2. Determination of mean values and uncertainties for each flux activity bin

For each bin i , we determined the mean value for flux activity $f_{Q,i}$ and its uncertainty $\sigma_{f_{Q,i}}$ as:

$$f_{Q,i} = \sum_j f_{Q,j} / N_i, \quad (S6)$$

$$\sigma_{f_{Q,i}} = \frac{\sqrt{\sum_j (f_{Q,j} - f_{Q,i})^2}}{\sqrt{N_i}}, \quad (S7)$$

where $f_{Q,j}$ are the individual values of flux activity in the bin and N_i is the total number of values in the bin. Eq. S7 was computed based on the typical formulation for the standard error [Eq. 4.14 in *Bevington and Robinson, 2003*]. Similarly, the mean effective threshold wind speed $u_{th,i}$ and its uncertainty $\sigma_{u_{th,i}}$ are:

$$u_{th,i} = \sum_j u_{th,j} / N_i, \quad (S8)$$

$$\sigma_{u_{th,i}} = \frac{\sqrt{\sum_j (u_{th,j} - u_{th,i})^2}}{\sqrt{N_i}}, \quad (S9)$$

where $u_{th,j}$ are the individual values of effective threshold in the bin.

S3.3. Estimation of uncertainties on effective threshold shear velocity and shear stress

We converted binned values for effective threshold wind speed $u_{th,i}$ to effective threshold shear velocity $u_{*,th}$ by Eq. 6 and to effective threshold stress τ_{th} by Eq. 7. Using the error propagation

formula [Eq. 3.14 in *Bevington and Robinson, 2003*], we propagated effective threshold wind speed uncertainty $\sigma_{u_{th}}$ and roughness length uncertainty σ_{z_0} (calculated in Supporting Information Text S4 below) to derive uncertainty in threshold shear velocity $\sigma_{u_{*,th}}$ and threshold stress $\sigma_{\tau_{th}}$:

$$\sigma_{u_{*,th}} = \frac{u_{*,th}}{u_{th}} \sqrt{\sigma_{u_{th}}^2 + \frac{\ln^2(\sigma_{z_0})}{\ln^2(z_u/z_0)} u_{*,th}^2}, \quad (\text{S10})$$

$$\sigma_{\tau_{th}} = 2\rho_f u_{*,th} \sigma_{u_{*,th}}. \quad (\text{S11})$$

Text S4. Determination of aerodynamic roughness height and its sensitivity to variation in saltation activity

Here, we describe methods for determining aerodynamic roughness height z_0 . Then we evaluate the possibility of systematic variation in saltation-influenced effective roughness height z_s with transport activity f_Q . To evaluate sensitivity of saltation-influenced von Karman parameter κ_s to f_Q , we assume that such von Karman sensitivity will be reflected in the sensitivity of z_s .

S4.1. Estimation of aerodynamic roughness height z_0

Under neutrally stable conditions with negligible saltation, the aerodynamic roughness height z_0 describes the zero-intercept height of a linear fit to the vertical profile of horizontal wind versus the logarithm of wind height. In practice, we found that wind profile fits to calculate z_0 showed very large variability due to large deviations from expected logarithmic law-of-the-wall profiles resulting from convective instability during periods of non-saltation (see Fig. 4 in *Martin et al.* [2016]).

To avoid the problem of unstable profiles, we instead considered the trend in effective roughness height z_s , which is influenced both by aerodynamic conditions and by saltation-induced roughness [*Sherman*, 1992], versus total saltation flux Q . (Methods for estimating Q are described in *Martin and Kok* [2016] and *Martin et al.* [2016].) For successive 30-minute intervals, we estimated z_s by manipulating the law-of-the-wall:

$$z_s = z_U \exp\left(-\frac{\kappa \bar{u}}{u_{*,Re}}\right), \quad (\text{S12})$$

where \bar{u} is the mean wind speed for anemometer height z_U during the 30-minute interval, $\kappa = 0.4$ is the von Karman parameter, and $u_{*,Re}$ is the shear velocity determined from the Reynolds stress method [*Martin and Kok*, 2016]. We calculated z_s by Eq. S12 over 30-minute intervals, instead of the $\Delta t = 1$ minute analysis intervals applied elsewhere in this paper, because $u_{*,Re}$ is ill-defined for $\Delta t = 1$ minute [*van Boxel et al.*, 2004].

Fig. S4 shows the variation in z_s with Q for each site. The logarithm of z_s increases linearly with Q up to $Q \approx 30 \text{ gm}^{-1}\text{s}^{-1}$. Performing a linear fit to $\ln(z_s)$ versus Q over this range, we estimate z_0 as the zero-intercept value of this fit, yielding values of $0.707 \times 10^{-4} \text{ m}$, $1.420 \times 10^{-4} \text{ m}$, and $0.995 \times 10^{-4} \text{ m}$, for Jericoacoara, Rancho Guadalupe, and Oceano, respectively. Associated uncertainties in log-space, i.e. $\sigma_{\ln(z_0)}$, are 0.115, 0.137, and 0.127, for Jericoacoara, Rancho Guadalupe, and Oceano, respectively.

S4.2. Sensitivity of effective roughness height z_s to changes in saltation activity f_Q

Values of z_0 as determined above were used for conversion of threshold wind speed u_{th} to threshold shear velocity $u_{*,th}$ and shear stress τ_{th} as described in Eqs. 6 and 7. However, such use of z_0 for this conversion may have failed to account for increase in the effective roughness length z_s with saltation intensity, thereby leading to underestimation of $u_{*,th}$ as compared to actual values.

To evaluate whether variation in z_s could have influenced our results, we directly compared measured values of f_Q over 30-minute intervals. Such comparison was only possible at Oceano, where 30-minute values of f_Q covered the full range of activities from 0 to 1. The result of this

comparison is shown in Fig. S5. Notably, there appears to be no significant variation in z_s with f_Q . We confirm this lack of trend by performing a linear fit to $\ln(z_s)$ versus f_Q . The best fit for this slope, -0.016 ± 0.185 , indicates a statistically insignificant trend. Though such a result seems at odds with the obvious increase in z_s with Q (Fig. S4), we note that most intermittent transport, i.e., $0.05 < f_Q < 0.95$, corresponds to relatively small saltation fluxes, for which the deviation of z_s away from z_0 is negligible.

S4.3. Sensitivity of effective von Karman parameter κ_s to changes in saltation activity f_Q

We did not directly evaluate sensitivity of κ_s to f_Q . Instead, we note that κ_s and z_s should display similar sensitivities to f_Q . Therefore, the lack of trend in z_s with f_Q suggests a lack of trend in κ_s with f_Q .

Text S5. Calculation of fluid and impact threshold stresses and shear velocities

To calculate fluid and impact threshold stresses, τ_{ft} and τ_{it} , at each field site, we performed linear fits to τ_{th} versus f_Q according to Eq. 5. Here, we detail the fitting procedure to obtain τ_{ft} , τ_{it} , and the uncertainty for these values. Then, we describe the calculation of the threshold shear velocity ratio and its uncertainty.

S5.1. Calculation of fluid and impact thresholds by linear fit to saltation activity versus effective threshold stress

Following Eqs. 6.12, 6.21, 6.22, and 7.23 in Bevington and Robinson [2003], we performed a linear fit to τ_{th} versus f_Q , i.e.,

$$\tau_{th} = a + bf_Q, \quad (\text{S13})$$

where a is the fitting intercept and b is the fitting slope; σ_a , σ_b , and σ_{ab}^2 are their respective uncertainties and covariance.

Based on the linear fit (Eq. S13), fluid and impact thresholds were calculated for each site from the best fit values corresponding respectively to $f_Q = 0$ and $f_Q = 1$, i.e.:

$$\tau_{ft} = a, \quad (\text{S14})$$

$$\tau_{it} = a + b. \quad (\text{S15})$$

Corresponding uncertainties in these values were then computed as:

$$\sigma_{\tau_{ft}} = \sigma_a, \quad (\text{S16})$$

$$\sigma_{\tau_{it}} = \sqrt{\sigma_a^2 + \sigma_b^2 + 2\sigma_{ab}^2}. \quad (\text{S17})$$

S5.2. Calculation of impact/fluid threshold shear velocity ratio and its uncertainty

The ratio of impact and fluid threshold shear velocities and the uncertainty of this ratio were calculated from τ_{ft} , τ_{it} , $\sigma_{\tau_{ft}}$, and $\sigma_{\tau_{it}}$ by error propagation [Eq. 3.14 in Bevington and Robinson, 2003] as:

$$\frac{u_{*it}}{u_{*ft}} = \sqrt{\frac{\tau_{it}}{\tau_{ft}}}, \quad (\text{S18})$$

$$\sigma_{u_{*it}/u_{*ft}} = \frac{1}{2} \sqrt{\frac{\sigma_{\tau_{it}}^2}{\tau_{it}\tau_{ft}} + \frac{\sigma_{\tau_{ft}}^2 \tau_{it}}{\sigma_{\tau_{ft}}^3}}. \quad (\text{S19})$$

Text S6. Chi-square tests for saltation activity control hypotheses

Here, we evaluate the quality of fluid $f_{Q,ft}$ (Eq. 1), impact $f_{Q,it}$ (Eq. 2), and dual $f_{Q,dual}$ (Eq. 3) threshold control predictions for saltation activity versus observations f_Q . To do so, we compute the reduced chi-square χ_v^2 , which expresses the difference between predicted and measured values, normalized by the number of degrees of freedom v :

$$\chi_v^2 = \frac{1}{v} \sum_i \frac{(f_{Q,i} - f_{Q,pred,i})^2}{\sigma_{f_{Q,pred,i}}^2}, \quad (\text{S20})$$

where the $f_{Q,i}$ refer to individual binned observations for saltation activity, the $f_{Q,pred,i}$ refer to the predictions by Eqs. 1-3, and the $\sigma_{f_{Q,pred,i}}$ are the standard errors for these predictions.

Because there are no fitting parameters for $f_{Q,pred,i}$ values, we set v simply as the number of $f_{Q,i}$ bins. The resulting χ_v^2 values for fluid $f_{Q,ft}$, impact $f_{Q,it}$, and dual $f_{Q,dual}$ threshold control are respectively: 149.6, 105.8, and 2.5 at Jericoacoara; 40.8, 42.1, and 3.1 at Rancho Guadalupe; and 654.6, 776.4, and 62.5 at Oceano. These χ_v^2 values indicate the favorability of the $f_{Q,dual}$ prediction at all sites.

Text S7. Sensitivity of results to atmospheric and surface trends

In this section, we perform sensitivity analyses to indirectly consider the effects of variability of atmospheric and surface conditions on the determination of effective thresholds and limiting fluid and impact threshold values. To do this, we sort the data for Oceano in two ways: (1) by time of day, and (2) by date. Separating data by time of day is meant to capture diurnal variations in atmospheric and surface properties, such as atmospheric stability, humidity, and soil moisture. Separating data by date is meant to capture secular variations in grain size and sorting properties, as surface grain size tended to coarsen over time at Oceano.

S7.1. Sensitivity analysis by time of day

We separate the data into three components of the diurnal cycle that constituted most measured saltation flux at Oceano: 12-14h, 14-16h, and 16-18h. The resulting variation of effective threshold τ_{th} with transport activity f_Q is shown in Fig. S6, and corresponding limiting impact and fluid threshold values are given in Table S4. Though the three diurnal periods do show some variation in limiting fluid and impact threshold values, there is no systematic trend of increasing or decreasing thresholds through the course of the day. Furthermore, the separation between fluid and impact threshold is maintained throughout the day.

S7.2. Sensitivity analysis by date

We separate the data into three ranges of dates for which saltation flux was measured at Oceano: May 15-19, May 23-28, and June 1-4, 2015. The resulting variation of effective threshold τ_{th} with transport activity f_Q is shown in Fig. S7, and corresponding limiting impact and fluid threshold values are given in Table S5. Notably, there does appear to be an increase in τ_{th} , and resulting increase in τ_{ft} and τ_{it} , for the May 23-28 and June 1-4 periods. These increases in the thresholds correspond to a slight coarsening of median grain diameter during these periods (Table S5). This supports the notion that thresholds increase with grain diameter. In all cases, the trend of effective threshold τ_{th} decreasing with transport activity f_Q is maintained.

Text S8. List of variables

Below, we list all variables described in the manuscript. Typical units for variables are given in parentheses, if applicable.

S8.1. Variables in main text

τ = shear stress (Pa)

τ_{ft} = fluid threshold shear stress (Pa)

τ_{it} = impact threshold shear stress (Pa)

u_{*it}/u_{*ft} = shear velocity threshold ratio

τ_{th} = effective threshold stress (Pa)

f_Q = saltation transport activity

$u(t)$ = time series of horizontal wind speed (m/s)

u_{ft} = fluid threshold wind speed (m/s)

u_{it} = impact threshold wind speed (m/s)

$f_{Q,ft}$ = expected saltation activity for transport dominated by fluid threshold

$f_{Q,it}$ = expected saltation activity for transport dominated by impact threshold

$f_{Q,dual}$ = expected saltation activity for transport mediated by both fluid and impact thresholds

f_+ = fraction of time with $u \geq u_{ft}$

f_{\sim} = fraction of time with $u_{it} \leq u < u_{ft}$

f_{\downarrow} = fraction of time within $u_{it} \leq u < u_{ft}$ for which the most recent threshold crossing was a downward crossing of u_{ft}

u_{th} = effective threshold wind speed (m/s)

Φ_u = cumulative distribution of streamwise wind speed u

N = vertically integrated saltation particle counts rate (counts/s)

z_U = anemometer height above the sand surface (m)

δt = averaging time interval (s)

Δt = analysis time interval (minutes)

$u_{*,th}$ = effective threshold shear velocity (m/s)

κ = von Karman parameter

z_0 = aerodynamic roughness height (m)

z_s = effective roughness height, accounting for saltation-induced roughness (m)

ρ_f = air density (kg/m^3)

z/L = stability parameter

θ = angle of horizontal wind relative to dominant sand-transporting wind

Q = saltation flux (g/m/s)

τ_0 = bed surface shear stress (Pa)

$\tau_{th,flux}$ = flux-based estimate of threshold stress (Pa)

S8.2. Additional variables in Supporting Information

f_D = saltation detection rate

$f_{Q|D}$ = probability that transport is actually active when it has been detected

$f_{D|Q}$ = conditional probability of detecting transport when it is active

$f_{\sim D|Q}$ = conditional probability of not detecting transport when it is active

λ = average arrival rate of particles (counts/s)

\bar{N} = mean vertically integrated saltation particle counts rate (counts/s)
 $f_{Q,i}$ = mean value for saltation transport activity for bin i
 $\sigma_{f_{Q,i}}$ = uncertainty in saltation transport activity for bin i
 $f_{Q,j}$ = individual values j of saltation activity in bin i
 N_i = number of values in bin i
 $u_{th,i}$ = mean value for effective threshold wind speed for bin i (m/s)
 $\sigma_{u_{th,i}}$ = uncertainty in effective threshold wind speed for bin i (m/s)
 $u_{th,j}$ = individual values j of effective threshold wind speed in bin i (m/s)
 $\sigma_{u_{*,th}}$ = uncertainty in effective threshold shear velocity (m/s)
 $\sigma_{\tau_{th}}$ = uncertainty in effective threshold shear stress (Pa)
 \bar{u} = 30-minute mean wind speed (m/s)
 $\sigma_{\ln(z_0)}$ = natural log uncertainty in aerodynamic roughness height
 κ_s = effective von Karman parameter, accounting for saltation effects
 a = least squares linear fitting intercept
 σ_a = uncertainty in fitting intercept
 b = least squares linear fitting slope
 σ_b = uncertainty in fitting slope
 σ_{ab}^2 = covariance of fitting slope and intercept
 $\sigma_{\tau_{ft}}$ = uncertainty in fluid threshold stress (Pa)
 $\sigma_{\tau_{it}}$ = uncertainty in impact threshold stress (Pa)
 $\sigma_{u_{*it}/u_{*ft}}$ = uncertainty in shear velocity threshold ratio
 ν = number of degrees of freedom for fitting
 χ^2_ν = normalized chi-square value for goodness of fit
 $f_{Q,pred,i}$, predicted value of saltation activity for bin i
 d_{50} , median diameter of surface particles by volume (mm)

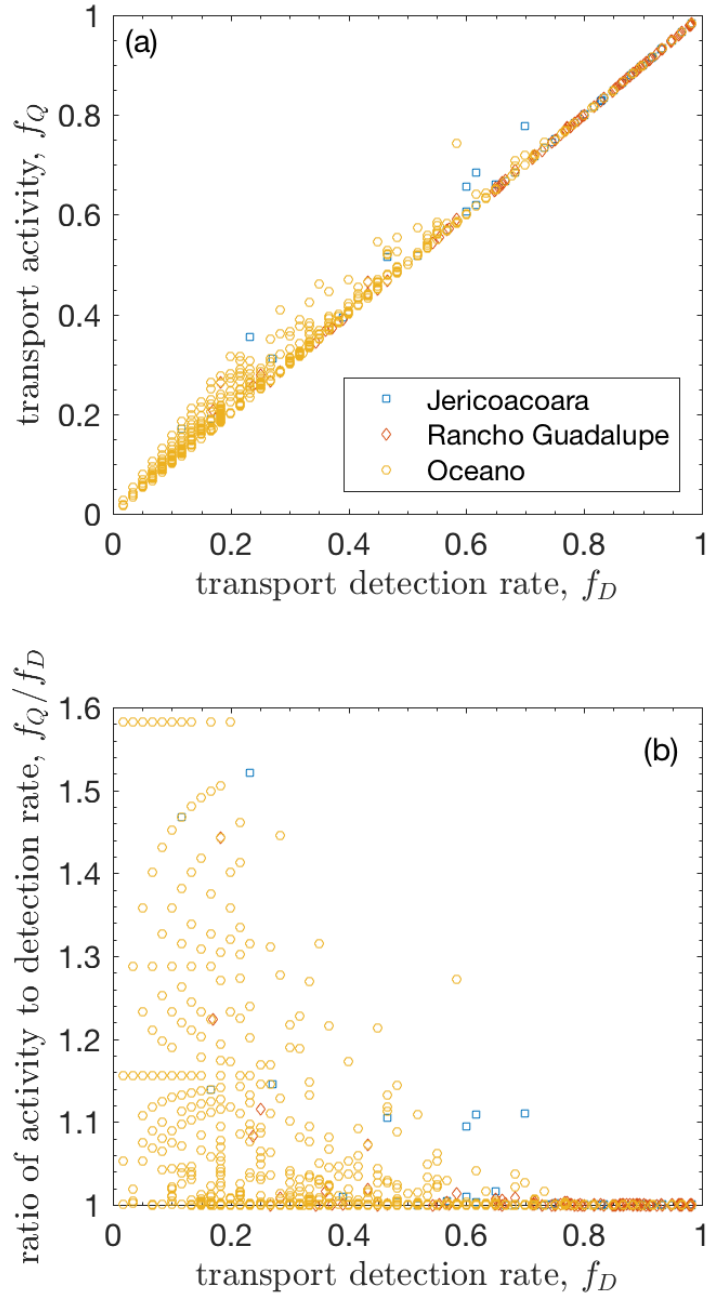


Figure S1. (a) Comparison of transport activity f_Q , which includes correction for estimated rate of false negatives (Eq. S5), to the actual transport detection rate f_D . (b) Ratio of transport activity to detection rate f_Q/f_D versus detection rate f_D , illustrating the relative magnitude of the correction for false negatives. This correction tends to be strongest when transport is weak, due to the higher probability of false negatives. The difference between f_Q and f_D is also affected by changes in the background particle detection rate, which can be affected by the number and height of Wenglor detectors and the nature of transport fluctuations.

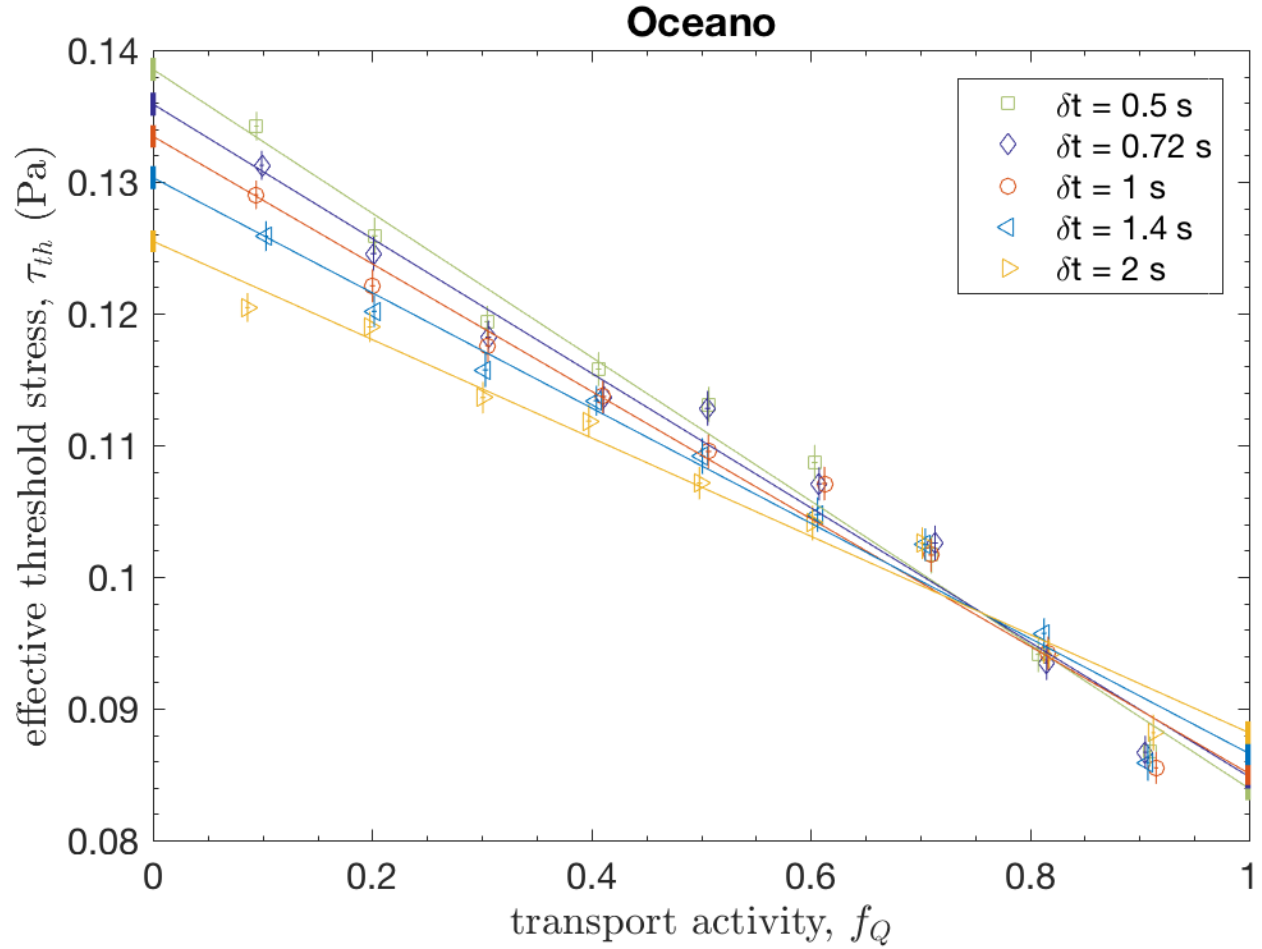


Figure S2. Comparison of effective threshold τ_{th} and transport activity f_Q for five averaging intervals δt at Oceano. Analysis interval Δt was fixed at 1 minute for this analysis. Limiting fluid and impact threshold values, indicated by vertical bars at $f_Q = 0$ and $f_Q = 1$, respectively, are given in Table S2.

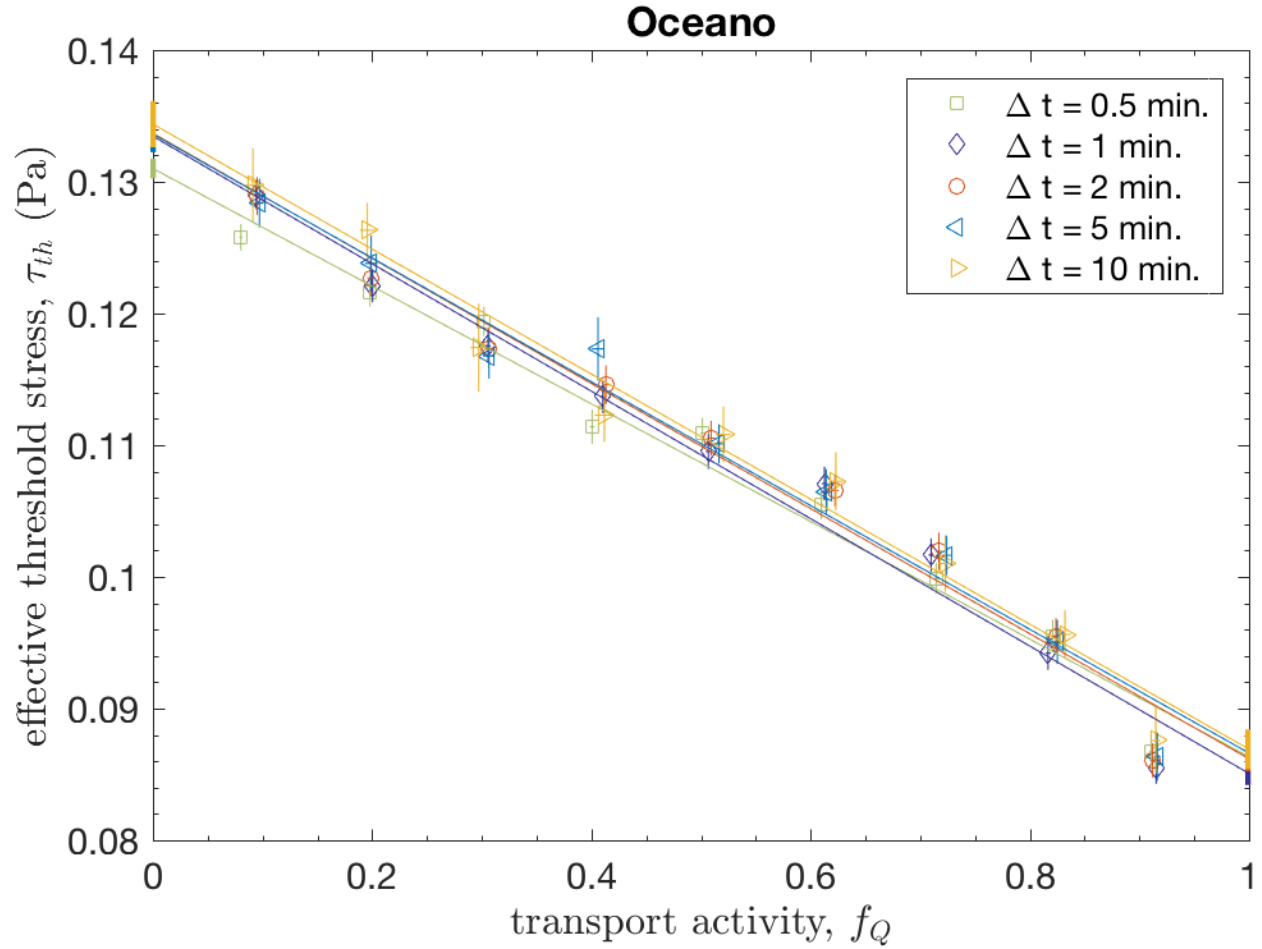


Figure S3. Comparison of effective threshold τ_{th} and transport activity f_Q for five different analysis intervals Δt at Oceano. Averaging interval δt was fixed at 1s for this analysis. Limiting fluid and impact threshold values, indicated by vertical bars at $f_Q = 0$ and $f_Q = 1$, respectively, are given in Table S3.

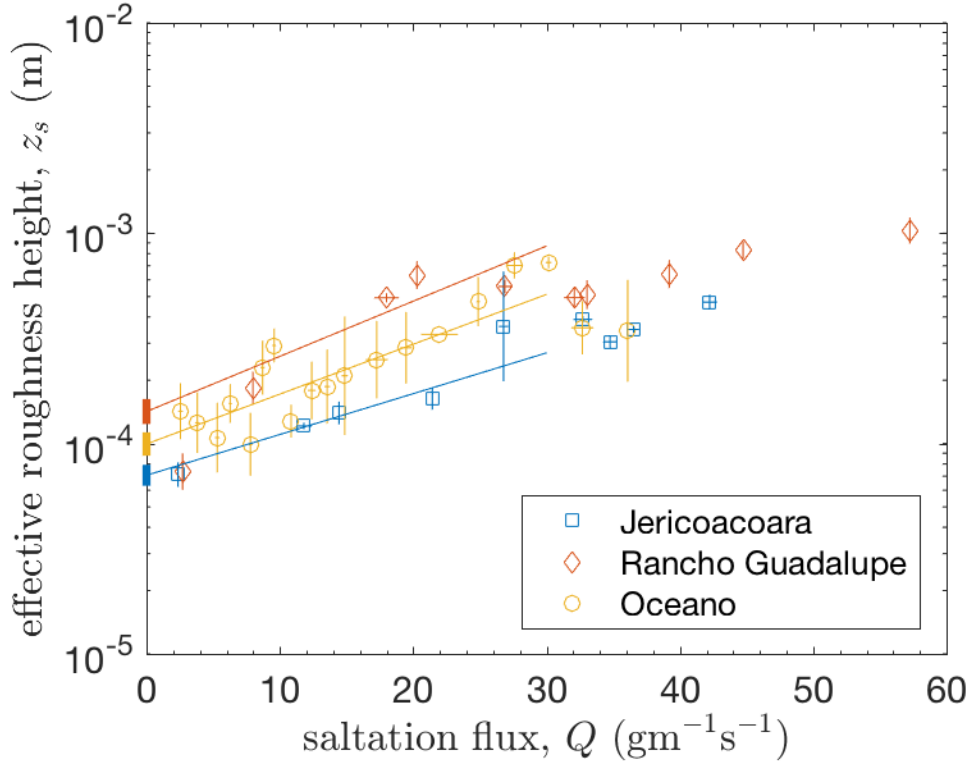


Figure S4. Comparison of effective roughness length z_s versus total saltation flux Q at each field site. We estimate z_0 as the zero-intercept of the linear fit of $\ln(z_s)$ versus Q at each site for $Q \leq 30 \text{ gm}^{-1}\text{s}^{-1}$, indicated by the thin lines. Resulting calculated z_0 values for each site are shown as thick vertical bars at $Q = 0 \text{ gm}^{-1}\text{s}^{-1}$. The vertical range of these bars corresponds to uncertainties in z_0 as determined by the linear fits.

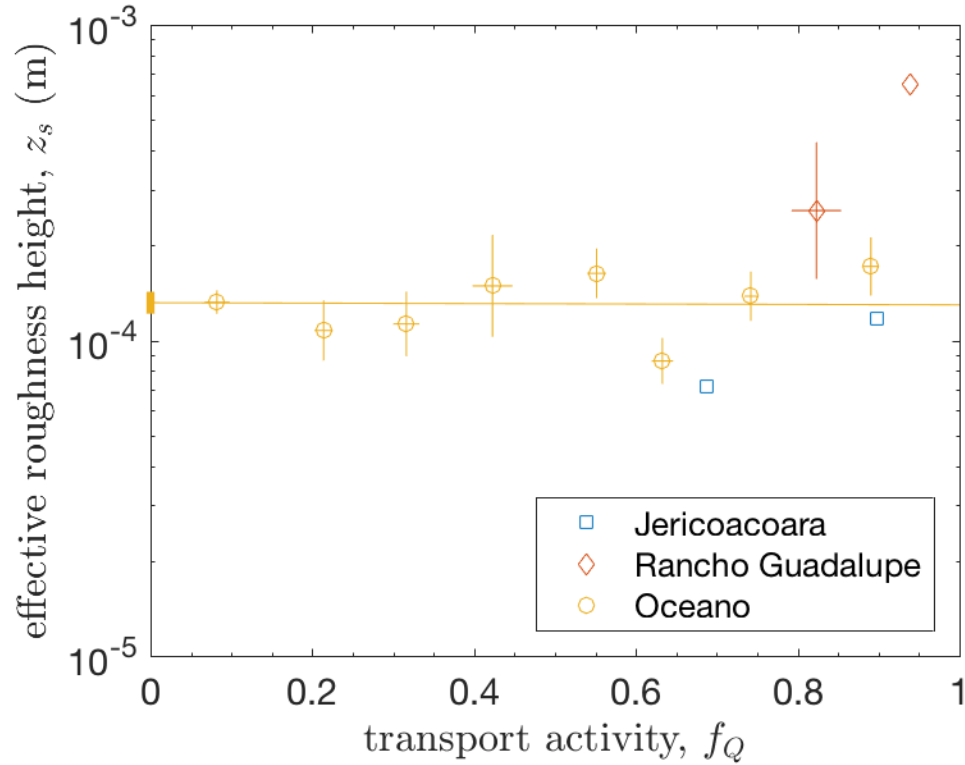


Figure S5. Comparison of effective roughness height z_s versus transport activity f_Q for intermittent transport ($0.05 < f_Q < 0.95$). Values are calculated over 30-minute intervals and combined into bins by f_Q . Ranges of 30-minute f_Q values as Jericoacoara and Rancho Guadalupe were insufficient for binning and fitting.

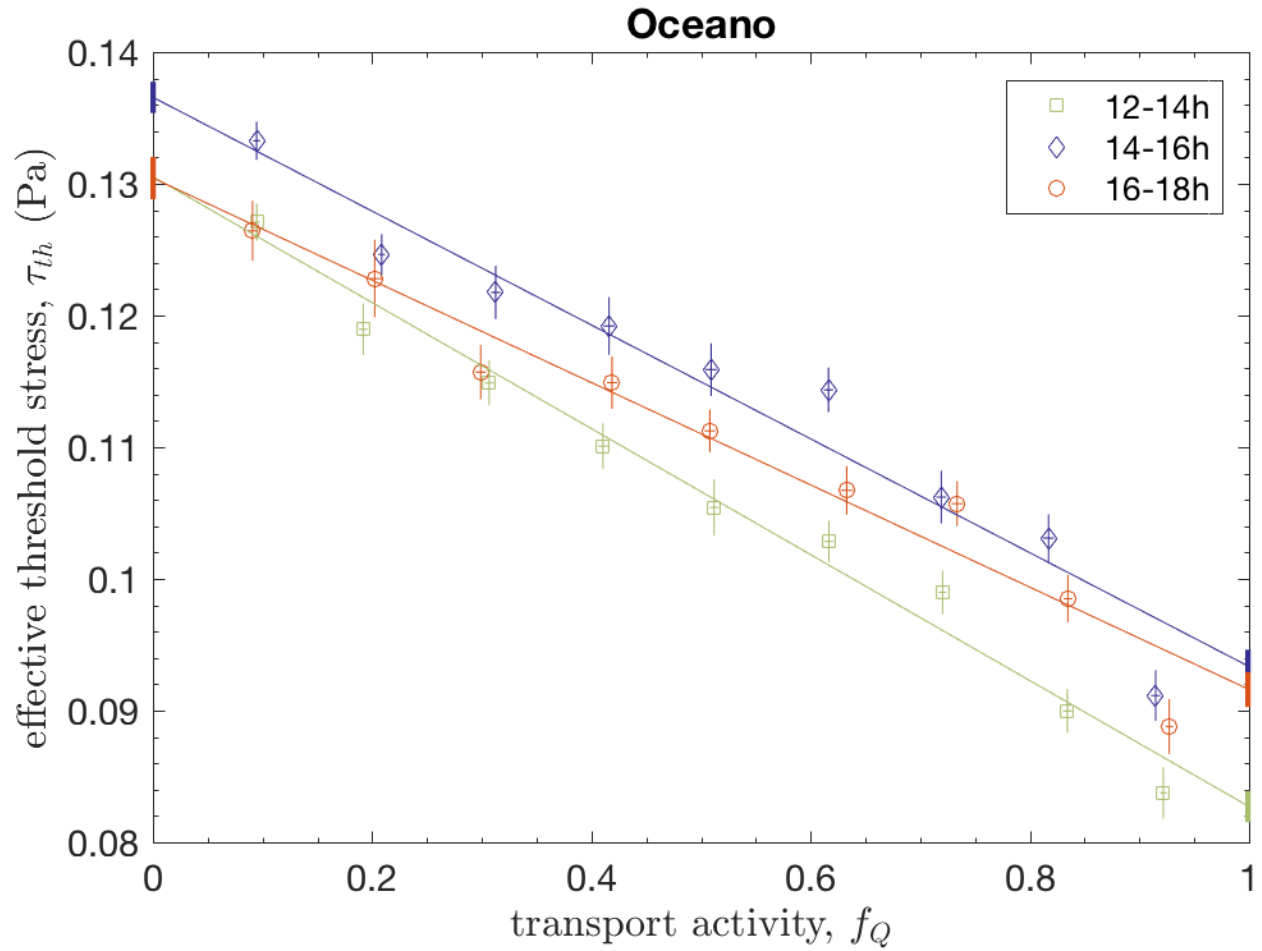


Figure S6. Comparison of effective threshold τ_{th} and transport activity f_Q for three different time periods for the diurnal cycle at Oceano. Limiting fluid and impact threshold values, indicated by vertical bars at $f_Q = 0$ and $f_Q = 1$, respectively, are given in Table S4.

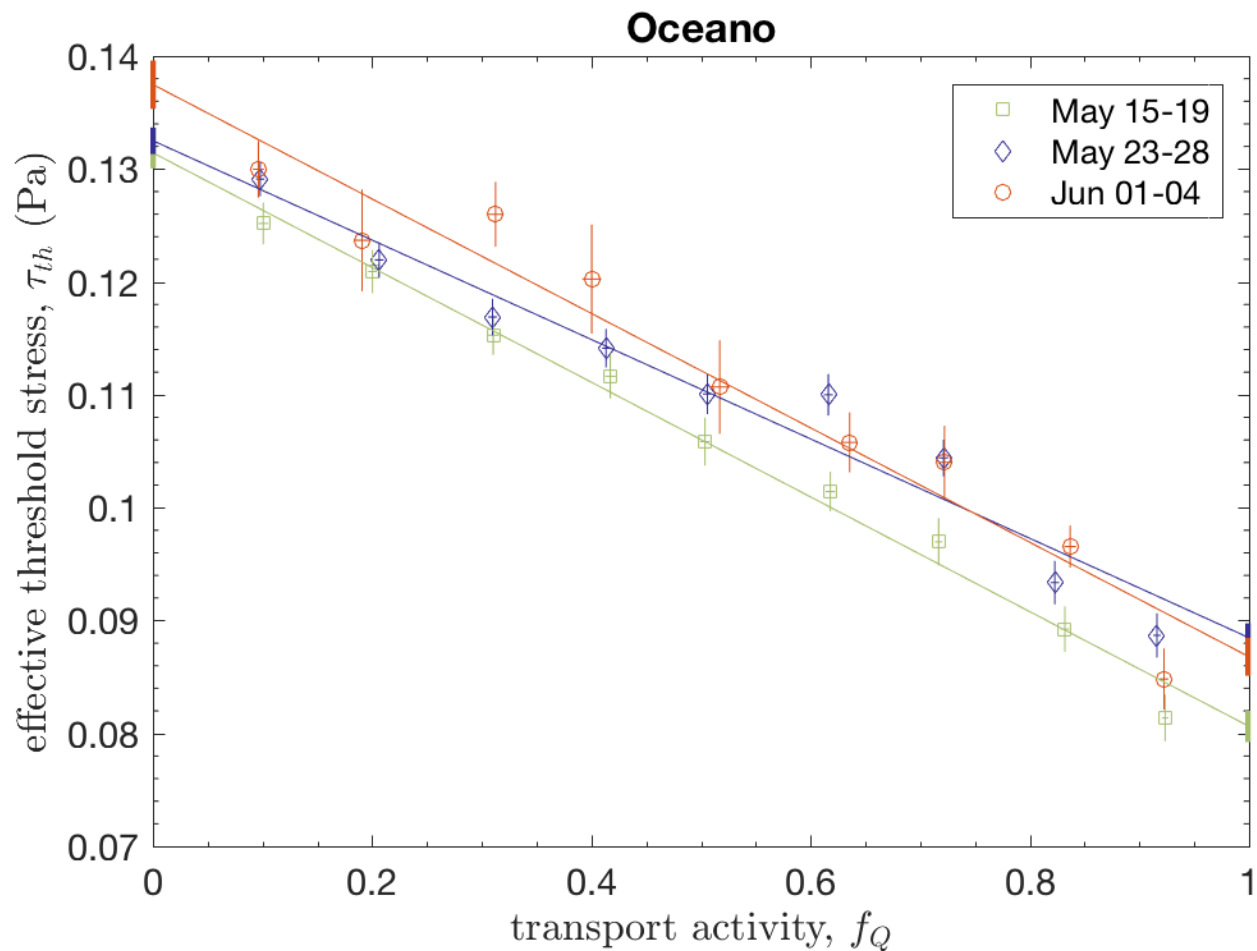


Figure S7. Comparison of effective threshold τ_{th} and transport activity f_Q for three segments of the deployment at Oceano, for which median surface grain diameter was respectively $d_{50} = 0.35$ mm, 0.42 mm, and 0.42 mm. Limiting fluid and impact threshold values, indicated by vertical bars at $f_Q = 0$ and $f_Q = 1$, respectively, are given in Table S5.

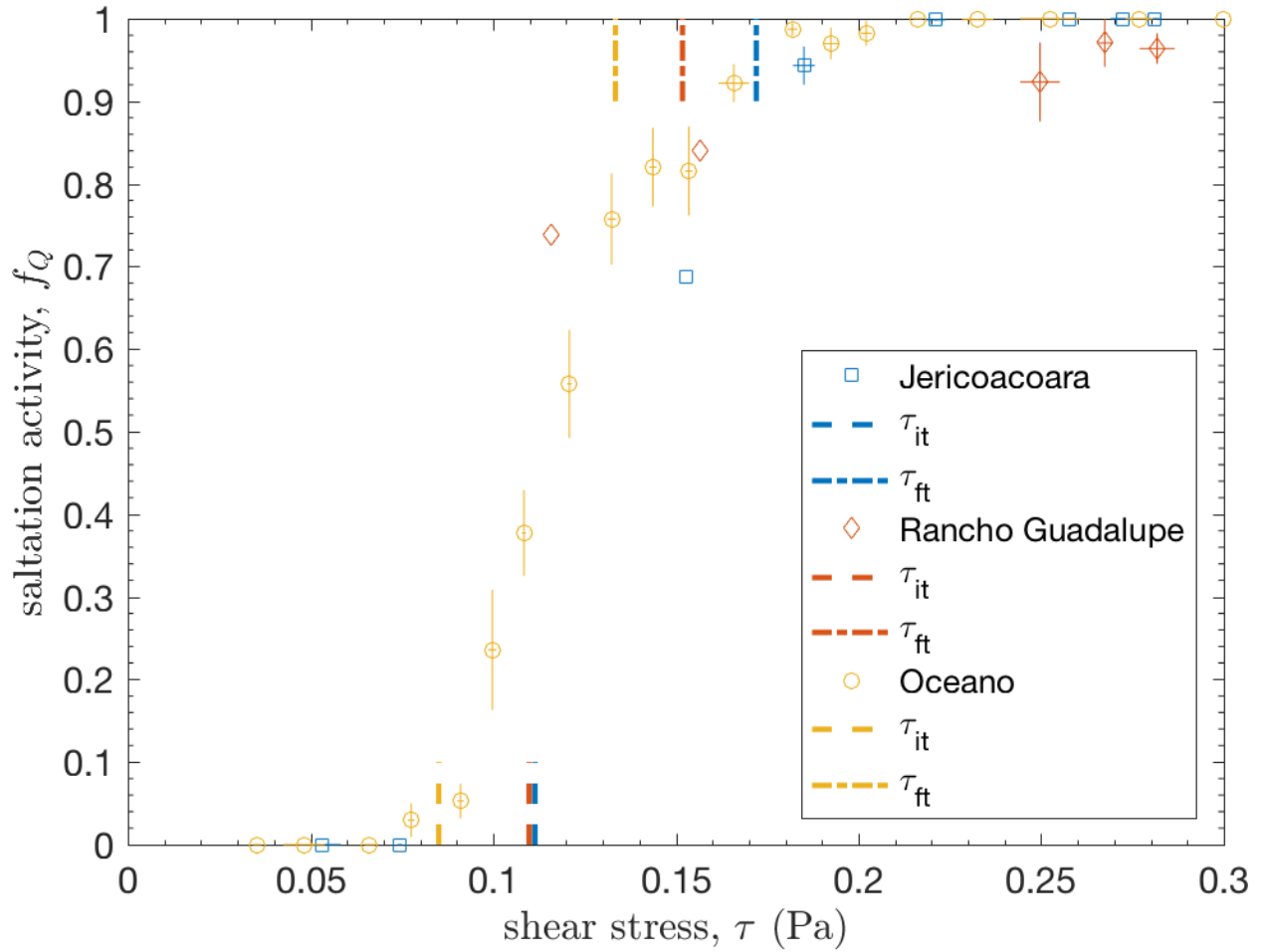


Figure S8. Saltation activity f_Q versus Reynolds shear stress τ . Values are computed over 30-minute intervals and combined into bins by range of τ . Error bars indicate standard error for each bin. Some values of $\tau > 0.3$, for which $f_Q = 1$, are not shown for clarity of the figure. Dashed lines indicate impact threshold τ_{it} and fluid threshold τ_{ft} at each site from Fig. 3.

Table S1. Threshold values for primary analysis with $\delta t = 1$ s averaging interval and $\Delta t = 1$ minute analysis interval. Median surface grain diameter of surface particles at each site is also included for reference.

Site	Median grain diameter, d_{50} (mm)	Fluid threshold stress, τ_{ft} (Pa)	Impact threshold stress, τ_{it} (Pa)	Threshold ratio, $u_{*,it}/u_{*,ft}$	Threshold from flux-law fit, $\tau_{th,flux}$ (Pa)
Jericoacoara	0.526 ± 0.037	0.172 ± 0.002	0.111 ± 0.002	0.805 ± 0.013	0.135 ± 0.015
Rancho Guadalupe	0.533 ± 0.026	0.152 ± 0.005	0.110 ± 0.002	0.851 ± 0.021	0.110 ± 0.021
Oceano	0.398 ± 0.070	0.133 ± 0.001	0.085 ± 0.001	0.798 ± 0.008	0.090 ± 0.007

Table S2. Best fit values for averaging interval δt sensitivity analysis at Oceano shown in Fig. S2. Uncertainties correspond to linear fitting uncertainty, which accounts for uncertainty in individual data points used for fitting.

Averaging interval, δt (s)	Fluid threshold, τ_{ft} (Pa)	Impact threshold, τ_{it} (Pa)	Threshold ratio, $u_{*,it}/u_{*,ft}$
0.5	0.139±0.001	0.084±0.001	0.778±0.008
0.72	0.136±0.001	0.085±0.001	0.790±0.008
1	0.133±0.001	0.085±0.001	0.799±0.008
1.4	0.130±0.001	0.087±0.001	0.815±0.008
2	0.125±0.001	0.088±0.001	0.838±0.007

Table S3. Best fit values for the sensitivity analysis of the analysis interval Δt , shown in Fig. S3 for Oceano.

Analysis interval, Δt (minutes)	Fluid threshold, τ_{ft} (Pa)	Impact threshold, τ_{it} (Pa)	Threshold ratio, $u_{*,it}/u_{*,ft}$
0.5	0.131 \pm 0.001	0.086 \pm 0.001	0.812 \pm 0.007
1	0.133 \pm 0.001	0.085 \pm 0.001	0.798 \pm 0.008
2	0.134 \pm 0.001	0.086 \pm 0.001	0.803 \pm 0.008
5	0.134 \pm 0.001	0.087 \pm 0.001	0.805 \pm 0.011
10	0.134 \pm 0.002	0.088 \pm 0.002	0.804 \pm 0.014

Table S4. Best fit values for diurnal cycle sensitivity analysis shown in Fig. S6 for Oceano.

Diurnal time interval	Fluid threshold, τ_{ft} (Pa)	Impact threshold, τ_{it} (Pa)	Threshold ratio, $u_{*,it}/u_{*,ft}$
12-14h	0.131 \pm 0.001	0.083 \pm 0.001	0.796 \pm 0.011
14-16h	0.137 \pm 0.001	0.093 \pm 0.001	0.827 \pm 0.010
16-18h	0.130 \pm 0.002	0.092 \pm 0.001	0.838 \pm 0.011

Table S5. Best fit values for date interval sensitivity analysis shown in Fig. S7 for Oceano. Median surface grain diameters d_{50} are also provided for these date intervals.

Date interval	Median grain diameter, d_{50}	Fluid threshold, τ_{ft} (Pa)	Impact threshold, τ_{it} (Pa)	Threshold ratio, $u_{*,it}/u_{*,ft}$
May 15-19	0.346±0.053	0.131±0.001	0.081±0.001	0.783±0.013
May 23-28	0.417±0.056	0.132±0.001	0.088±0.001	0.817±0.010
June 1-4	0.415±0.074	0.137±0.002	0.087±0.002	0.795±0.016